Geochemistry Geophysics Geosystems G3
AN ELECTRONIC JOURNAL OF THE EARTH SCIENCES
Published by AGU and the Geochemical Society

Article
Volume 10, Number 12
29 December 2009
Q12017, doi:10.1029/2009GC002892
ISSN: 1525-2027

Volcanic and geochemical evolution of the Teno massif, Tenerife, Canary Islands: Some repercussions of giant landslides on ocean island magmatism

Marc-Antoine Longpré
Department of Geology, Trinity College Dublin, College Green, Dublin 2, Ireland

Now at Earth and Planetary Sciences, McGill University, 3450 University Street, Montreal, Quebec H3A 2A7, Canada (m-a.longpre@mcgill.ca)

Valentin R. Troll
Department of Geology, Trinity College Dublin, College Green, Dublin 2, Ireland

Now at Department of Earth Sciences, Uppsala Universitet, Villavägen 16, SE-752 36 Uppsala, Sweden

Thomas R. Walter
GeoForschungsZentrum Potsdam, Telegrafenberg, D-14473 Potsdam, Germany

Thor H. Hansteen
Leibniz-Institut für Meereswissenschaften an der Universität Kiel (IFM-GEOMAR), Wischhofstrasse 1-3, D-24148 Kiel, Germany

[1] Large-scale, catastrophic mass wasting is a major process contributing to the dismantling of oceanic intraplate volcanoes. Recent studies, however, have highlighted a possible feedback relationship between flank collapse, or incipient instability, and subsequent episodes of structural rearrangement and/or renewed volcano growth. The Teno massif, located in northwestern Tenerife (Canary Islands), is a deeply eroded Miocene shield volcano that was built in four major eruptive phases punctuated by two lateral collapses, each removing >20–25 km^3 of the volcano's north flank. In this paper, we use detailed field observations and petrological and geochemical data to evaluate possible links between large-scale landslides and subsequent volcanism/magmatism during Teno's evolution. Inspection of key stratigraphic sequences reveals that steep angular unconformities, relics of paleolandslide scars, are marked by polymict breccias. Near their base, these deposits typically include abundant juvenile pyroclastic material, otherwise scarce in the region. While some of Teno's most evolved, low-density magmas were produced just before flank collapses, early postlandslide lava sequences are characterized by anomalously high proportions of dense ankaramite flows, extremely rich in clinopyroxene and olivine crystals. A detailed sampling profile shows transitions from low-Mg # lavas relatively rich in SiO_2 to lavas with low silica content and comparatively high Mg # after both landslides. Long-term variations in Zr/Nb, normative nepheline, and La/Lu are coupled but do not show a systematic correlation with stratigraphic boundaries. We propose that whereas loading of the growing precollapse volcano promoted magma stagnation and differentiation, the successive giant landslides modified the shallow volcano-tectonic stress field at Teno, resulting in widespread pyroclastic eruptions and shallow magma reservoir drainage. This rapid unloading of several tens of km^3 of near-surface rocks appears to have upset magma differentiation processes, while facilitating the remobilization and tapping of denser ankaramite magmas that were stored in the uppermost mantle. Degrees of mantle melting coincidently reached a maximum in the short time interval between the two landslides and declined shortly after, probably reflecting intrinsic plume processes rather than

a collapse-induced influence on mantle melting. Our study of Teno volcano bears implications for other oceanic volcanoes where short-term compositional variations may also directly relate to major flank collapse events.

Components: 16,575 words, 12 figures, 4 tables.

Keywords: Canary Islands; Tenerife; Teno; giant landslides; volcano evolution; pyroclastic eruptions.

Index Terms: 3615 Mineralogy and Petrology: Intra-plate processes (1033, 8415); 3621 Mineralogy and Petrology: Mantle processes (1038); 3690 Mineralogy and Petrology: Field relationships (1090, 8486).

Received 7 October 2009; **Revised** 14 October 2009; **Accepted** 21 October 2009; **Published** 29 December 2009.

Longpré, M.-A., V. R. Troll, T. R. Walter, and T. H. Hansteen (2009), Volcanic and geochemical evolution of the Teno massif, Tenerife, Canary Islands: Some repercussions of giant landslides on ocean island magmatism, *Geochem. Geophys. Geosyst.*, *10*, Q12017, doi:10.1029/2009GC002892.

1. Introduction

[2] Lateral collapse, or incipient flank instability, can dramatically affect the behavior of a volcano. This is best exemplified by the 18 May 1980 eruption of Mount Saint Helens, where the sliding of a rockslide debris avalanche block unroofed and decompressed a shallow magma intrusion (cryptodome) and its surrounding hydrothermal system, resulting in the initial explosions of a lateral blast [*Glicken*, 1996, and references therein]. The Mount Saint Helens landslide, although catastrophic, remains an event of relatively small magnitude ($\sim$2.5 km^3 [*Glicken*, 1996, and references therein]) when compared to some of the largest landslides on Earth, which take place on oceanic intraplate volcanoes and exceed 1000 km^3 in some cases [e.g., *Moore et al.*, 1994; *Masson et al.*, 2002].

[3] Giant landslides are now viewed as normal occurrences within the lifespan of virtually all oceanic shield volcanoes [*McGuire*, 1996, and references therein]. Catastrophic mass wasting contributes largely to volcano dismantling, surpassing the effect of long-term erosion and, at least in the case of the Canarian volcanoes, that of subsidence [e.g., *Moore et al.*, 1994; *Carracedo et al.*, 1998; *Gee et al.*, 2001]. On the other hand, giant mass wasting may cause an isostatic rebound [*Smith and Wessel*, 2000] and several authors have reported rapid constructional phases following collapse that are generally concentrated in the landslide source regions, e.g., on the islands of Hawaii (Mauna Loa volcano) [*Lipman et al.*, 1991], La Palma (Bejenado volcano) [*Carracedo et al.*, 1999a], Fogo (Pico do Fogo volcano) [*Day et al.*, 1999], Tahiti-Nui (northern depression) [*Hildenbrand et al.*, 2004], La Gomera (Garajonay embayment) [*Paris et al.*, 2005b] and La Réunion (Piton de la Fournaise volcano) [*Oehler et al.*, 2008].

[4] Feedback processes between flank instability and magma plumbing have been documented at both extinct and active volcanoes and may result in the reconfiguration of existing rift zones and ultimately promote the formation of new rift arms [*Lipman et al.*, 1991; *Day et al.*, 1999; *Walter and Schmincke*, 2002; *Tibaldi*, 2004; *Walter et al.*, 2005a, 2005b]. In addition, *Amelung and Day* [2002] proposed that giant lateral collapses may lead to the removal or extinction of preexisting shallow magma reservoirs. Yet other studies suggest that large-scale landsliding may also affect the geochemical regime of ocean island volcanoes. Apparent increases in the degree of partial melting in the mantle have been attributed to collapse-induced decompression [*Presley et al.*, 1997; *Hildenbrand et al.*, 2004]. A direct link between the significant reduction of overburden during mass wasting and apparent subsequent adjustments of the magmatic system has thus been repeatedly inferred in the literature, but lacks in-depth testing at natural examples.

[5] In this paper, we use the late Miocene Teno volcano on the island of Tenerife as a type example, where it appears that volcanism was markedly affected by the occurrence of two successive giant landslides. Detailed field observations, and the combination of new and published petrographic and geochemical data, improve our knowledge on Teno's volcanic evolution and reveal that not only did the large flank collapses influence the eruptive regime, but also the deep magma plumbing system of the volcanic edifice.

2. Geological Background

[6] There is now wide acceptance that the Canary Islands, like Hawaii, owe their origin to a mantle hot spot, although substantial debate on the matter

has taken place until recently [*Holik et al.*, 1991; *Hoernle and Schmincke*, 1993a, 1993b; *Carracedo et al.*, 1998; *Anguita and Hernán*, 2000]. Unlike Hawaii, however, the Canary Islands are built close to a continental margin on one of the oldest seafloors on Earth and on a near-stationary plate, which result in a slow volcanic propagation rate [e.g., *Carracedo et al.*, 1998].

[7] As in Hawaii, each island of the Canary Archipelago represents the product of coalescing volcanoes [e.g., *Carracedo et al.*, 2001; *Guillou et al.*, 2004]. While each Hawaiian volcano typically grows through four stages (i.e., the preshield, shield, postshield and rejuvenated (or posterosional) stages [*Clague and Dalrymple*, 1987]), a two-step evolution (i.e., the shield stage and rejuvenated stage) is most readily identifiable in the Canary Islands, although equivalents of the four Hawaiian stages have also been proposed to occur [cf. *Carracedo et al.*, 1998; *Paris et al.*, 2005b]. Most of the major peculiarities of Canarian volcanoes with respect to "archetypal" hot spot volcanoes (e.g., Hawaii, La Réunion, Society) may be explained by the greater lithospheric thickness, lower plume flux and, especially, slower plate motion [see *Hoernle and Schmincke*, 1993b; *Carracedo et al.*, 1998]. However, some features of Canarian volcanism, such as multiple magmatic cycles on a single island and a historic eruption on one of the oldest, easternmost island (Lanzarote), remain difficult to reconcile with a simple, continuously active mantle plume. *Hoernle and Schmincke* [1993a] proposed that the Canary hot spot is characterized, from 100 to 200 km depth, by a broad region of upwelling (>600 km long and >200 km wide), where "blobs" of plume material rise beneath the islands. In this model, the decompression melting of a single blob produces a discrete magmatic cycle, in which the saturation of magmas in SiO_2 initially increases and then decreases.

[8] Tenerife, the largest and highest of the Canary Islands, was largely built between 11.9 and 3.9 Ma by the coalescence of independent shield volcanoes, with distinct magmatic sources [*Thirlwall et al.*, 2000]. The remnants of these volcanoes crop out in the Roque del Conde (South), Teno (NW) and Anaga (NE) massifs [*Ancochea et al.*, 1990; *Thirlwall et al.*, 2000; *Guillou et al.*, 2004] (Figure 1). The Roque del Conde massif, with radiometric dates between 11.9 and 8.9 Ma, represents the earliest stages of subaerial volcanism on Tenerife and is thought to be the only exposed part of a much larger Central shield [*Guillou et al.*, 2004]. The later Teno (between ~6.3 and ~5.0 Ma) and Anaga (between 4.9 and 3.9 Ma) shields emerged in the northwest and northeast parts of the present-day island, respectively [*Guillou et al.*, 2004; *Leonhardt and Soffel*, 2006]. Emissions from the Roque del Conde (Central shield), Teno and Anaga volcanoes are largely basaltic, with abundant alkali basalts and picrobasalts (often ankaramites), common basanites and less frequent, more evolved hawaiites, mugearites and benmoreites [*Thirlwall et al.*, 2000].

[9] Some 2 Ma of volcanic hiatus and erosion may have followed the last eruptions at Anaga before rejuvenated volcanism formed the voluminous Las Cañadas edifice in central Tenerife essentially between 1.9 and 0.2 Ma and the later twin stratovolcano complex, Teide-Pico Viejo after about 0.2 Ma [*Ancochea et al.*, 1990]. This rejuvenated volcanism, although varied in composition, is significantly more alkalic and presents much higher proportions of felsic products (phonolites) than the older basaltic shields [e.g., *Ablay et al.*, 1998]. The most recent eruption on Tenerife was basaltic in composition and took place on the Northwest Rift zone of the central edifices in 1909 [*Carracedo et al.*, 2007].

[10] Episodes of mass-wasting events, occurring as early as 6 Ma and as late as 150 ka, have affected the edifices of Teno, Anaga, and Las Cañadas [*Masson et al.*, 2002, and references therein] and most probably that of the Central shield as well [*Carracedo et al.*, 2007]. Cumulatively, these giant landslides removed more than 1000 km^3 of rock from the upper slopes of Tenerife's volcanic edifices [*Masson et al.*, 2002].

3. Stratigraphy of the Teno Massif

[11] The Teno massif reaches a maximum elevation in excess of 1,300 m above sea level at Cumbre Bolicos (Figure 2). Ridges, bounded by >200 m high cliffs, and eroded canyons ("barrancos"), ~500 m deep, expose most of the stratigraphic sequence. In the course of this study, we carefully reviewed previously published stratigraphic constraints for the Teno massif [*Ancochea et al.*, 1990; *Walter and Schmincke*, 2002; *Guillou et al.*, 2004; *Leonhardt and Soffel*, 2006; *Carracedo et al.*, 2007]. The main results of our analysis are shown in Figures 1–3 and summarized in Table 1, while the remaining details are outlined and discussed in the auxiliary material.[1] We essentially adopt a strati-

[1] Auxiliary materials are available in the HTML. doi:10.1029/2009GC002892.

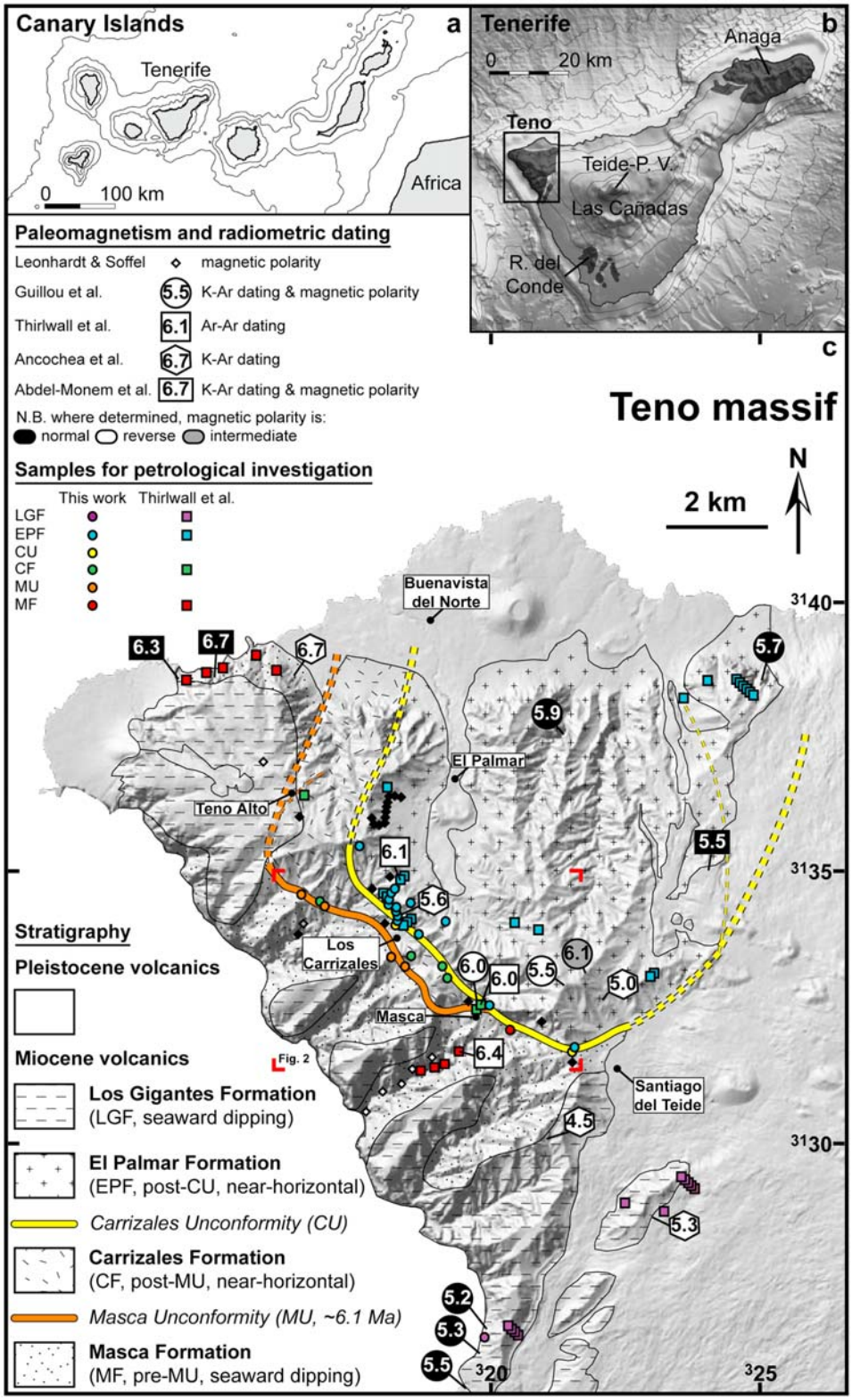

Figure 1. (a) The Canary Islands and the central position of Tenerife within the archipelago. (b) Map of Tenerife, showing the location of the Teno massif in the northwest of the island. (c) Geological map of the Teno massif, including data from *Walter and Schmincke* [2002], *Guillou et al.* [2004], *Carracedo et al.* [2007], and this study. Radiometric and paleomagnetic study sites are plotted. Sample locations for this work (circles) and *Thirlwall et al.* [2000] (squares) are color coded according to the stratigraphic formation to which they are assigned. UTM coordinate grid is shown; tick marks are spaced by 5 km. The area framed by red corners is enlarged in Figure 2.

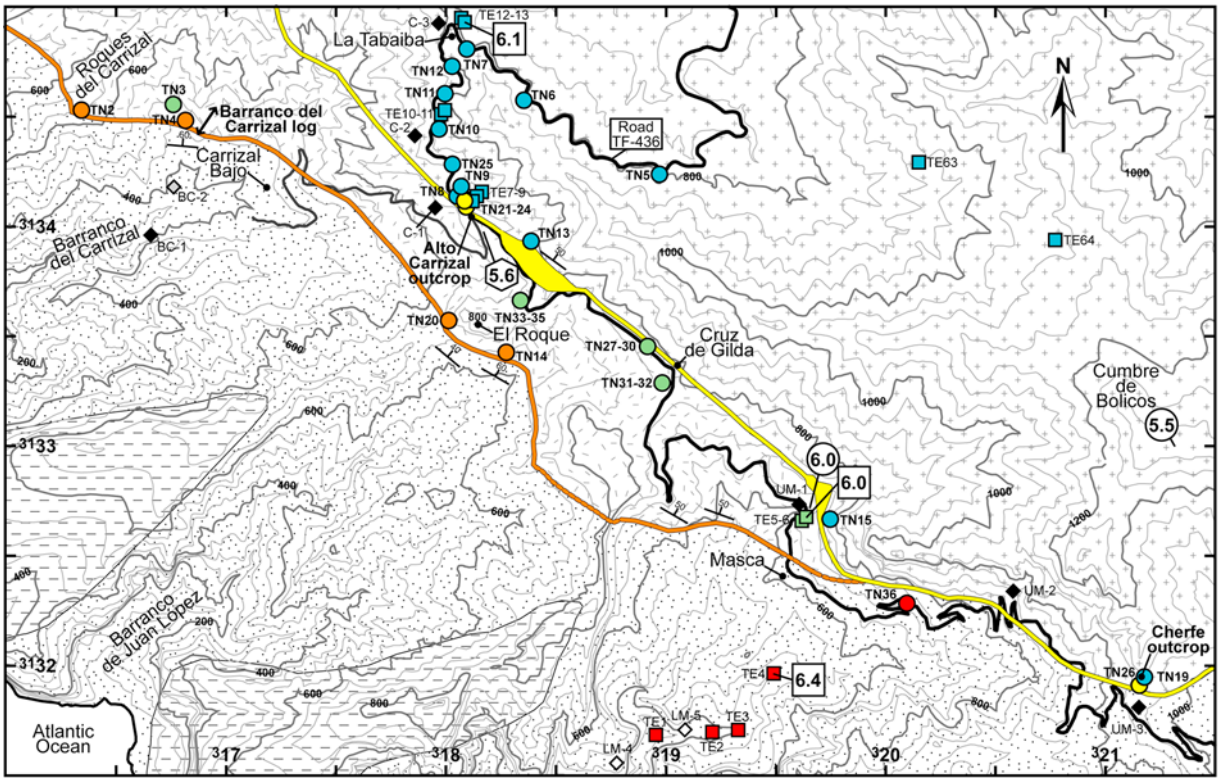

Figure 2. Topographic map (50 m contours) of the area enclosing road TF-436 between the Cherfe outcrop and La Tabaiba. All symbols are as in Figure 1. Sample names are indicated (see also Table 4), as well as key outcrop/stratigraphic profile localities discussed in section 4. Strike and dip symbols represent measured attitudes of the unconformities. UTM coordinate grid is shown; tick marks are spaced by 500 m.

graphic framework that only differs in detail from that proposed by *Leonhardt and Soffel* [2006]. The Masca Formation is defined as the oldest series of lavas, mostly exposed in the Barranco de Masca underlying the Masca unconformity. These lavas appear to have been largely extruded during the reverse polarity chron C3An.1r, from 6.27 to 6.14 Ma ago [see *Cande and Kent*, 1995]. Subsequently, a series of events are thought to have taken place during the normal polarity chron C3An.1n, lasting ~250 ka from 6.14 to 5.89 Ma ago. A first giant landslide, the Masca Collapse (forming the Masca Unconformity), was followed by the infill of the collapse embayment by the lavas of the Carrizales Formation. Then, a second landslide occurred, the Carrizales Collapse (forming the Carrizales Unconformity), this time followed by the extrusion of most of the lavas of the El Palmar Formation that accumulated inside the newly formed scar. After a possible hiatus in volcanic activity during the next reverse polarity chron, the youngest Miocene lavas in Teno were extruded during the normal polarity interval C3n.4n, from 5.23 to 4.98 Ma ago. These volcanics that overlie the Masca Formation without apparent unconformity and form the cliffs of Los Gigantes retain the name Los Gigantes Formation (Figures 1–3 and Table 1). A ~4 Ma gap in volcanic activity separates Los Gigantes eruptions from the Pleistocene volcanics that have been dated between 706 and 153 ka and interpreted as distal products of the Northwest Rift of the recent and active central edifices [*Carracedo et al.*, 2007].

4. Description of Stratigraphic Units

[12] In this section, we describe Teno's stratigraphic units with emphasis to temporal variations in the lithology and mineralogy of volcanic products, focusing on key outcrop localities and stratigraphic sections (Figures 4 and 5).

[13] Throughout our field evaluation, we used the modal mineralogy as the best discriminator for Teno lava types: (1) aphyric to subaphyric (<5 vol. % phenocrysts of plagioclase/clinopyroxene/olivine, called aphyric basalt), (2) plagioclase-phyric (5–40 vol. %, called plagioclase basalt, previous authors may have used the term "trachyte"), and (3) moderately clinopyroxene- and/or olivine-phyric (5–20 vol. %, called basalt) and highly

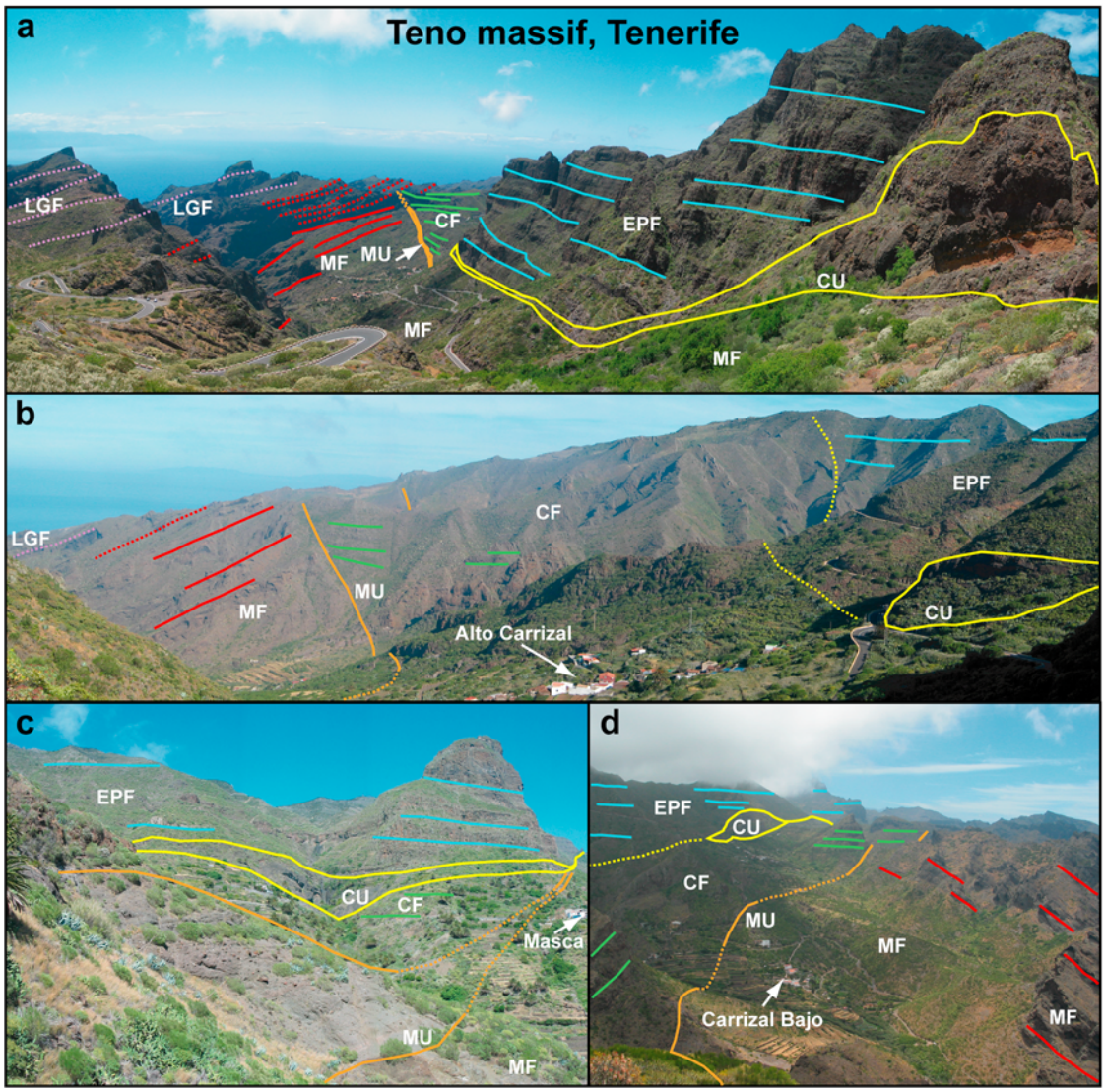

Figure 3. Unconformity-bounded stratigraphic formations of the Teno massif: MF, Masca Formation (red); MU, Masca Unconformity (orange); CF, Carrizales Formation (green); CU, Carrizales Unconformity (yellow); EPF, El Palmar Formation (blue); and LGF, Los Gigantes Formation (purple). (a) Photo (looking west) taken from near Cherfe outcrop in eastern Teno, before the descent of TF-436 toward Santiago del Teide. The exact position of the transition between the Masca and Los Gigantes formations is uncertain. (b) Photo (looking northwest) taken from near El Roque (Figure 2). The Masca Unconformity is particularly well observed from this point. (c) Photo (looking east) taken from the barranco just west of Masca village. The angular unconformities converge just above the village. (d) Photo (looking east-southeast) taken near TN2 sample locality (Figure 2). The steeply dipping volcanics of the Masca Formation are clearly seen on the right-hand side (south).

clinopyroxene-olivine-phyric (>20 vol. %, called ankaramite). Note that these names are used here, as in previous work on Teno, as field terms that do not imply a particular position in the total alkali-silica chemical classification diagram [e.g., *Le Maitre et al.*, 1989]. For primary volcaniclastic rocks, the descriptions are tied in to the classification scheme of *White and Houghton* [2006].

[14] Logging of key stratigraphic sections (Figure 5), with focus on the postcollapse Carrizales and El Palmar formations, was undertaken on the principle that the thickness of these near-horizontal lava flows (or group of flows) can be estimated with altitude readings. Absolute vertical position of lava piles may have been affected by postemplacement deformation (along deformation zones associated with the unconformities [see *Walter and Schmincke*, 2002]), but relative stratigraphic level has been preserved.

Table 1. Revised Stratigraphy for the Teno Massif[a]

Formation	Type Locality	K-Ar and Ar-Ar Ages (Ma)	Polarity Readings	Inferred Polarity Chron	Corresponding Age (Ma)
Los Gigantes	Los Gigantes cliffs	4.5,[b] 5.2,[c] 5.3,[b] 5.3,[c] 5.5[c]	N,[c] N,[c] N[c]	C3n.4n	4.980–5.230
	upper northwest Teno		R[d]	C3n.4r?	5.230–5.894?
El Palmar					
Upper	Cumbre Bolicos	5.0,[b] 5.5,[c] 6.1[c]	I,[c] R[c]	C3n.4r	5.230–5.894
Middle/lower	between Alto Carrizal and La Tabaiba	5.5,[e] 5.6,[b] 5.7,[c] 5.9,[c] 6.1[f]	N,[e] N,[c] N,[c] I,[d] 13 × N[d]	C3An.1n	5.894–6.137
Carrizales					
Upper/middle	from Masca village to Cruz de Gilda		N,[d] N[d]	beginning of C3An.1n	5.894–6.137
Lower	Barranco del Carrizal log and ~200 m north of Masca	6.0,[f] 6.0[c]	R,[c] N[d]	end of C3An.1r/ beginning of C3An.1n	6.137–6.269
Masca					
Upper	locality for sample TN36 and on road near Cherfe outcrop		N[d]	beginning of C3An.1n	5.894–6.137
Middle	Barranco de Masca	6.4[f]	5 × R[d]	C3An.1r	6.137–6.269
Lower	lower northwest Teno, Barranco del Carrizal	6.3,[e] 6.7,[e] 6.7[b]	N,[e] N,[e] N,[d] I[d]	end of C3An.2n	6.269–6.567

[a] K-Ar, Ar-Ar, and magnetostratigraphy sites of *Abdel-Monem et al.* [1972], *Ancochea et al.* [1990], *Thirlwall et al.* [2000], *Guillou et al.* [2004], and and *Leonhardt and Soffel* [2006] were plotted on Google Earth; this allowed their correct correlation with the corresponding stratigraphic formations defined in this study (see auxiliary material).
[b] *Ancochea et al.* [1990].
[c] *Guillou et al.* [2004].
[d] *Leonhardt and Soffel* [2006].
[e] *Abdel-Monem et al.* [1972].
[f] *Thirlwall et al.* [2000].

4.1. Masca Formation

[15] The Masca Formation consists predominantly of steeply seaward dipping, <1 m thick basaltic lava flows that are frequently clastic with minor scoria deposits, commonly intruded by numerous dikes [see also *Ancochea et al.*, 1990; *Walter and Schmincke*, 2002]. Most striking near the top of the Masca Formation, however, is the occurrence of a thick pyroclastic unit, anomalously felsic among Teno volcanics, which can be described as a thick vitric tuff with common lithics [cf. *White and Houghton*, 2006]. *Walter and Schmincke* [2002, p. 617] referred to it as a "80-m-thick glassy phonolitic agglutinate with discontinuous spatter lenses." This unit is best exposed at [320080, 3132280] (UTM coordinates, datum WGS84) and about 730 m of altitude, some 500 m east of Masca village along the road to Santiago del Teide, just below the Carrizales Unconformity (Figures 2 and 4a, sample TN36).

4.2. Masca Unconformity

[16] The Masca Unconformity is the oldest and southwesternmost of the two angular unconformities exposed in the Teno massif (Figures 1–3) and is generally marked by the occurrence of a 10–15 m thick polymict breccia [see also *Ancochea et al.*, 1990; *Walter and Schmincke*, 2002]. As noted by *Walter and Schmincke* [2002], the breccia, with modal decimetric blocks, is commonly found interbedded and sometimes mixed with lithified scoriaceous lapilli deposits (coarse to medium lapilli tuffs [cf. *White and Houghton*, 2006]). This can be observed at outcrops near [318250, 3133400], while larger blocks reaching ~2 m are found at the base of the breccia at [319280, 3132600]. As seen in Figure 4b, the lapilli tuffs are occasionally observed resting directly on older Masca lavas, with the breccia found a few meters higher up. The unconformity and the associated breccia and lapilli tuffs dip steeply, between 30°N and 60°N, depending on locality.

4.3. Carrizales Formation

[17] The Carrizales Formation, consisting mainly of near-horizontal lava flows, differs markedly from the older, steeply dipping Masca Formation (Figure 3). In comparison, it is intruded by fewer

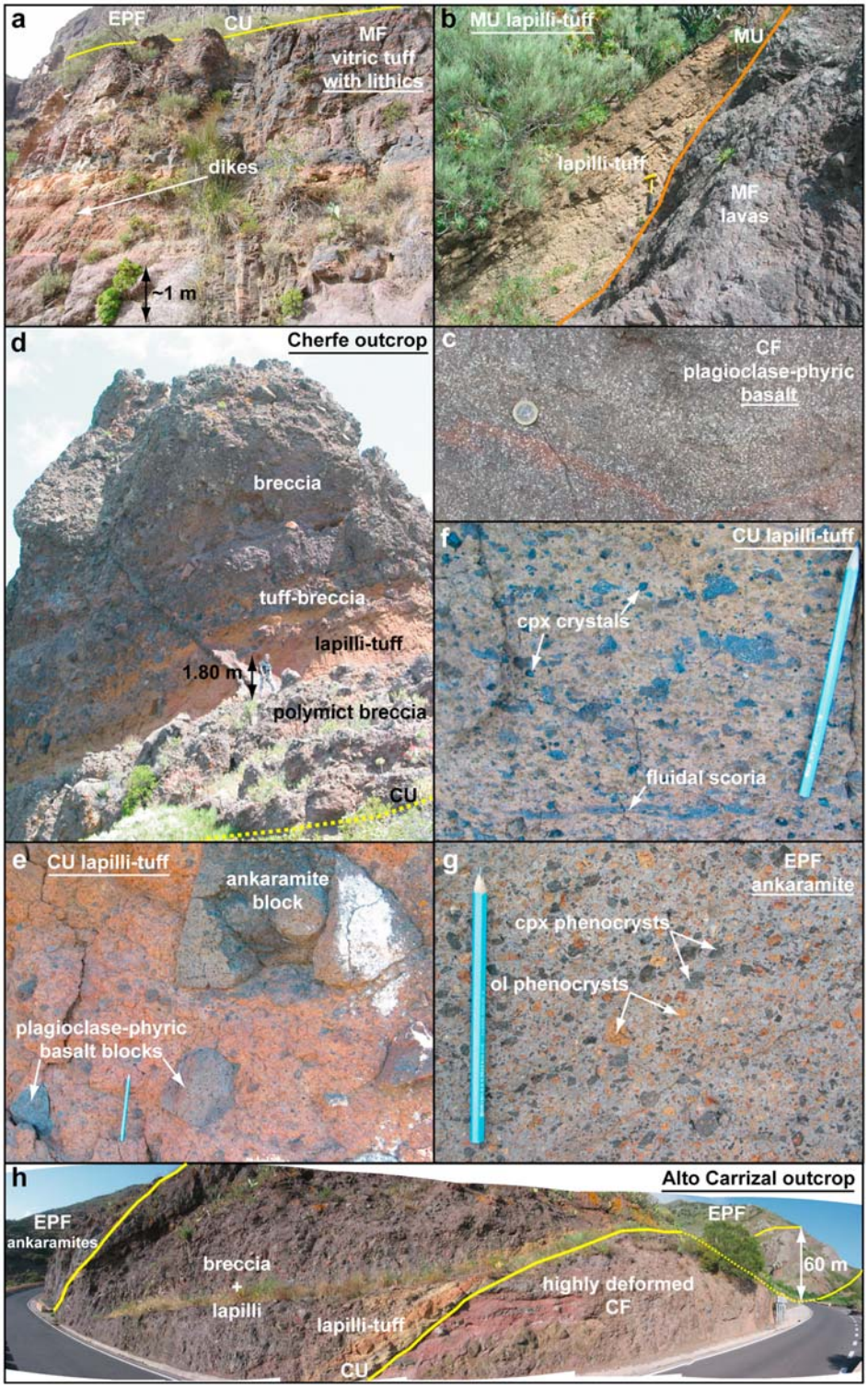

Figure 4. (a) The thick, felsic pyroclastic deposits near the top of the Masca Formation, being the sample location of TN36. (b) Juvenile pyroclastic deposit resting at the Masca Unconformity near El Roque. (c) Typical appearance of the plagioclase-phyric lavas of the upper Carrizales Formation. (d) The Cherfe outcrop, showing steeply dipping polymict breccias mixed and interbedded with lapilli tuffs, at the Carrizales Unconformity, eastern Teno. (e) At Cherfe outcrop. Lava blocks are incorporated into pyroclastic deposits. (f) Close-up of Cherfe pyroclastics, showing clinopyroxene crystals and fluidal scoria. (g) Representative example of lower El Palmar ankaramite lavas. (h) The Alto Carrizal outcrop, showing a complex sequence of highly deformed Carrizales rocks overlain by pyroclastic rocks and breccias of the Carrizales Unconformity, which are in turn overlain by El Palmar ankaramites.

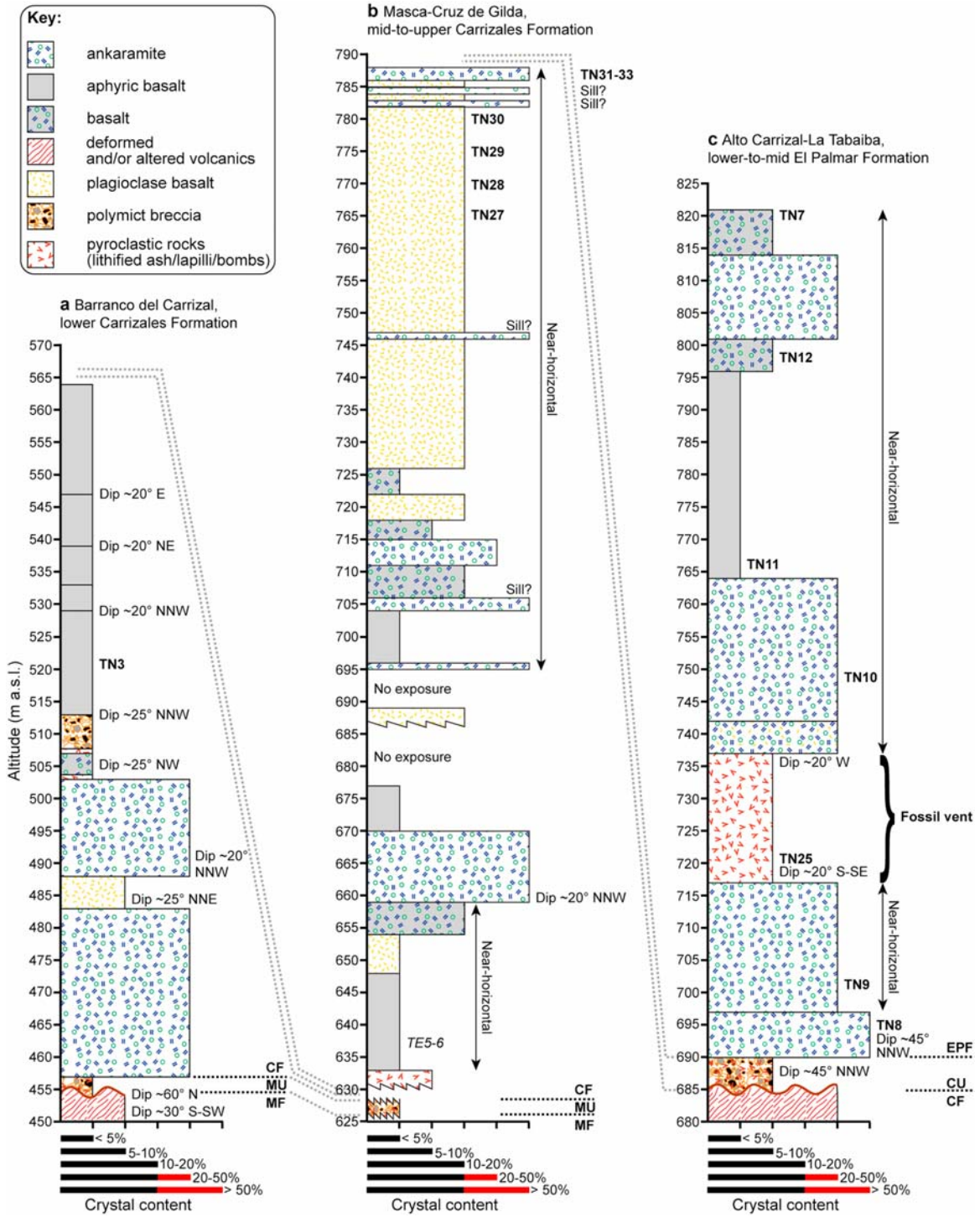

Figure 5. Logs of key stratigraphic sequences at Teno, with the crystal content of volcanic rocks and altitude as the *x* and *y* axes, respectively. For acronyms of formation names, see Figures 1 and 3. Approximate altitudes of notable stratigraphic boundaries were measured using a barometric altimeter built into a handheld GPS (calibrated to sea level, accuracy ±3 m, precision ±0.3 m). Note that lavas at the base of the postcollapse sequences typically dip approximately north. In these cases, values represent apparent thicknesses only. Overall, however, postcollapse formations consist of near-horizontal lavas. Sample localities for this work, as well as for TE5-6 of *Thirlwall et al.* [2000] (M. Thirlwall, personal communication, 2007), are indicated. (a) Section on the western slopes of Barranco del Carrizal, lower Carrizales Formation. (b) Section starting just north of Masca village and ending near Cruz de Gilda, middle to upper Carrizales Formation. (c) Section from the Alto Carrizal outcrop following road TF-436 toward La Tabaiba, lower to middle El Palmar Formation. See section 4 for further details.

dikes and is characterized by the virtual absence of pyroclastic rocks [see also *Ancochea et al.*, 1990; *Walter and Schmincke*, 2002; *Guillou et al.*, 2004]. Two main sections, where Carrizales rocks were found in contact with the Masca Unconformity, were investigated in more detail: (1) in the Barranco del Carrizal and (2) along road TF-436 between Masca village and the view point at Cruz de Gilda (Figure 2).

4.3.1. Barranco del Carrizal Log

[18] This section starts northwest of Carrizales Bajo, near [316840, 3134470] at an altitude of 460 m and continues up stratigraphy toward [316900, 3134540] at about 560 m above sea level (Figures 2 and 5a). At outcrops near the base of this log, the altered, purplish-blue clastic lavas of the Masca Formation are crosscut by the polymict breccia, with a thickness ranging from 4 to 5 m to <1 m, marking the Masca Unconformity. A 30–40 cm thick ash-rich layer, containing clinopyroxene phenocrysts, tops the steeply dipping (~60°N) breccia. Above this, the lowermost part of the Carrizales Formation is characterized by the abundance of ankaramite lava flows rich in large (some up to 3 cm across) olivine and clinopyroxene crystals [see also *Walter and Schmincke*, 2002]. These clastic lavas dip up to 25°N and are dominant up to an altitude of ~500 m, after which aphyric to subaphyric basalts are found until the top of the profile.

4.3.2. Masca–Cruz de Gilda Log

[19] At higher altitudes and stratigraphic level compared to Barranco del Carrizal, the Masca–Cruz de Gilda section corresponds to the middle to upper Carrizales Formation (Figure 5b). The geometry of the Masca Unconformity near Masca village (Figures 2 and 3c, see also auxiliary material) implies that Carrizales lavas crop out some 200 m north along the road at [319550, 3132600] and ~630 m of altitude, where reddish scoriaceous lapilli tuffs are overlain by an aphyric lava flow. Following road cut outcrops, the lower part of the sequence consists of clinopyroxene- and olivine-phyric lava flows, including several ankaramites. At altitudes around 720 m, however, thin (generally <50 cm thick) plagioclase-phyric lavas, with abundant elongated crystals up to 5 mm in length, become dominant until the top of the profile near Cruz de Gilda (samples TN27–30, Figures 4c and 5b). Volumetrically minor ankaramites (samples TN31–35, Figure 5b) top the sequence and outcrops of the Carrizales Unconformity breccia are seen only a few meters above the road. The combination of the Barranco del Carrizal and Masca–Cruz de Gilda logs entails a minimum thickness of ~200–300 m for the Carrizales lava pile (Figures 5a and 5b), although it may have been as thick as 700 m before it was truncated by the Carrizales Collapse [*Walter and Schmincke*, 2002].

4.4. Carrizales Unconformity

[20] The Carrizales Unconformity breccia is overall substantially thicker than that of the Masca Unconformity [see also *Walter and Schmincke*, 2002]. Near [318320, 3133850], an extensive outcrop implies thicknesses of up to ~45 m (Figure 2). At this locality, the breccia consists of moderately to poorly sorted clasts (2–200 cm) that appear to occur in several discrete beds inclined 40°–45° to the NNE, each a few meters thick.

[21] In eastern Teno, toward Santiago del Teide, the Carrizales Unconformity breccia is exposed near [321170, 3131910] at ~1090 m of altitude, where it dips ~30°–40°NW (Figures 2, 3a, and 4d–4f). Overall, this locality, herein called the Cherfe outcrop, can be described from base to top to grade from breccia, to lapilli tuff, to tuff breccia and back to breccia. At the outcrop base, the breccia has a purplish color, is poorly sorted and includes lapilli and scoriaceous lapilli as well as up to meter-sized blocks. The matrix is ash-rich, with dispersed clinopyroxene crystals and altered olivines. Up-section, the breccia matrix takes a yellow-orangey tone, due to the gradually increasing content of lapilli and ash. This is also accompanied by an increased concentration of clinopyroxene crystals. Eventually, a fine to medium lapilli tuff horizon dominated by orangey lapilli and ash, with subordinate lithic clasts and lava blocks (1–100 cm in size), is reached (Figure 4e). Dark scoria with fluidal shapes are also observed (Figure 4f). These clinopyroxene- and olivine-bearing (up to 15–20 vol. %) pyroclastic materials can be seen many meters up the steep, ~30 m high outcrop, but decrease in abundance upward as lava blocks become dominant again.

4.5. El Palmar Formation

[22] The El Palmar Formation is composed of a thick pile of near-horizontal (dip < 5°N) lavas that directly overlies the Carrizales Unconformity (Figures 1–3). Where in contact with the unconformity, El Palmar rocks are found at their lowest stratigraphic level near 690 m of altitude. These lavas, however, are found at lower elevations in the

El Palmar valley (Figure 1), although this may not correspond to lower stratigraphic level. Cumbre Bolicos, the highest point of the Teno massif, marks the top of this formation, giving it an approximate thickness in excess of 600–700 m (Figure 2).

4.5.1. Alto Carrizal Outcrop

[23] The Alto Carrizal outcrop (near [318140, 3134040], junction of road TF-436 and secondary road to Los Carrizales village) exposes the details of the transition between the Carrizales Formation, the Carrizales Unconformity and the overlying El Palmar Formation (Figures 2, 4g, and 4h). The southeasternmost part of the outcrop (at the lowest stratigraphic position) consists of highly deformed (some boudinage-like deformation) and altered Carrizales Formation ankaramitic rocks, intruded by several dikes. A sharp contact (dip ~45°NNW) with a 50 to 100 cm thick yellowish lapilli tuff bed marks the unconformity. The tuff contains dark, fluidal, fiamme-like features and sparse clinopyroxene and olivine phenocrysts in an ash-rich matrix. This layer grades into a ~5 m thick mixture of polymict breccia and pyroclasts, which vary in proportions. This is sharply overlain by fine-grained to scoriaceous lapilli tuffs (still NNW dipping, ~1 m total thickness) that contain increasing amounts of clinopyroxene and olivine crystals. This is in turn covered by a sequence of north dipping ankaramite lava flows of the El Palmar Formation.

4.5.2. Alto Carrizal–La Tabaiba Log

[24] Figure 5c shows the stratigraphic sequence logged from the Alto Carrizal outcrop to La Tabaiba (Figure 2), following the main road up to ~825 m elevation and spanning ~135 m of stratigraphic thickness. The lowest El Palmar lavas along this road cut are 5 ankaramite flows, each 5–6 m in thickness (their steep north dip result in lower apparent thickness shown in Figure 5c), with abundant scoria near their tops. These are followed by a sequence of near-horizontal, columnar ankaramite lavas (Figure 4g). At an altitude of 715 m near [318011, 3134201], lithified lapilli, scoria and bombs intruded by several dikes define the conical geometry of a fossil vent (Figure 5c). Further along the road, the pyroclastics rocks are overlain by additional ankaramite lavas up to ~765 m of altitude. The first aphyric or subaphyric lava flows of the El Palmar Formation along this profile are then encountered and dominate the rest of the stratigraphic sequence up to La Tabaiba, with the exception of some ankaramite lavas near 800 m of altitude.

4.6. Los Gigantes Formation

[25] Although this formation may largely be equivalent to the upper El Palmar Formation [cf. *Guillou et al.*, 2004], it occurs outside the paleolandslide embayment defined by the Carrizales Unconformity; it forms the outermost portions of the massif with the Los Gigantes cliffs as the type locality (Figures 1–3). The formation consists mainly of gently seaward dipping (10–25°S to SW) lavas of varying composition (plagioclase basalt to ankaramite) and some reddish scoriaceous lapilli tuffs [cf. *Walter and Schmincke*, 2002]. Los Gigantes lavas seem broadly concordant on top of the significantly older Masca Formation; this resulted previously in some confusion about the stratigraphic sequence in southern and western Teno (Figures 3a and 3b, see also auxiliary material) [*Walter and Schmincke*, 2002; *Guillou et al.*, 2004; *Leonhardt and Soffel*, 2006].

5. Petrology and Geochemistry

[26] The major and trace element chemistry and its implications for magma petrogenesis at the basaltic shields of Tenerife are widely discussed by *Thirlwall et al.* [2000]. Here, we follow on these authors' detailed work and provide complementary information, especially in the light of the newly established stratigraphic framework. Unaltered lava samples were systematically collected from the main profile extending from Masca village to La Tabaiba (Figures 2, 5b, and 5c), as well as from some other key localities, spanning a total stratigraphic height of ca. 650 m. Pyroclastic rocks were also sampled for petrographic examination (see auxiliary material), but, with the exception of the unaltered sample TN36, were not used for geochemical analyses due to their advanced state of hydration. Whole-rock major and trace element compositions were obtained for all unaltered samples by X-Ray Fluorescence (XRF) (Table 2). In addition, groundmass material of ankaramite samples was extracted, crushed, melted and quenched; the glass produced was subsequently analyzed by electron microprobe (EMP) (Table 2). Rare earth element (REE) concentrations were determined by ICP mass spectrometry on seven selected whole-rock samples (Table 3). Further details of analytical procedures and uncertainties are outlined in the auxiliary material. Note that major element oxide compositions, including the data for Teno samples

Table 2. Major and Trace Element Composition of Whole-Rock and Fused Groundmass Samples[a]

	Sample																				
	TN1			TN3,	TN5			TN6, wr	TN7			TN8			TN9			TN10			TN11,
	wr	fg	σ	wr	wr	fg	σ		wr	fg	σ	wr	fg	σ	wr	fg	σ	wr	fg	σ	wr
SiO_2	44.38	45.50	0.57	45.38	44.30	45.63	0.38	42.23	43.98	44.98	1.05	43.18	44.18	0.57	44.40	45.54	0.63	44.32	44.64	0.68	42.44
TiO_2	3.42	3.85	0.19	4.30	2.25	3.32	0.13	3.82	3.44	3.76	0.17	3.54	4.03	0.16	3.36	3.56	0.23	2.56	3.45	0.11	3.96
Al_2O_3	14.61	16.26	0.29	16.31	9.59	14.03	0.12	14.98	15.14	16.87	0.36	14.02	15.68	0.20	15.48	16.80	0.22	10.95	14.36	0.19	15.09
FeO_t	12.95	12.50	0.28	12.90	12.58	11.88	0.21	12.94	11.81	11.62	0.16	12.72	12.49	0.30	12.17	12.09	0.17	12.53	12.45	0.41	13.39
MnO	0.18	0.18	0.02	0.19	0.17	0.18	0.03	0.18	0.17	0.19	0.03	0.17	0.19	0.06	0.17	0.21	0.05	0.17	0.18	0.04	0.18
MgO	8.19	5.94	0.11	4.32	17.02	9.45	0.11	5.72	7.25	5.57	0.10	9.82	7.95	0.08	6.89	6.21	0.09	14.34	8.44	0.13	5.48
CaO	10.41	10.23	0.09	9.33	10.99	12.17	0.11	11.72	10.69	10.25	0.13	10.44	10.76	0.10	10.70	10.02	0.09	11.66	12.35	0.12	11.67
Na_2O	3.15	3.50	0.19	3.07	1.59	2.59	0.11	3.08	3.65	4.23	0.16	2.34	2.64	0.08	2.92	3.36	0.04	1.88	2.90	0.05	2.44
K_2O	1.23	1.20	0.10	1.22	0.59	0.85	0.04	1.27	1.14	1.22	0.10	1.14	0.95	0.06	1.26	1.33	0.03	0.69	0.91	0.05	1.22
P_2O_5	0.61	0.25	0.14	0.65	0.25	0.22	0.06	0.74	0.71	0.40	0.24	0.62	0.12	0.03	0.59	0.38	0.12	0.30	0.30	0.10	0.74
Total	99.13	99.42		97.67	99.33	100.33		96.68	97.98	99.08		97.99	99.00		97.94	99.49		99.40	99.97		96.61
LOI	0.79			1.28	0.44			1.75	2.08			1.89			1.86			0.50			1.53
Co	67			44	90			50	51			59			51			74			54
Cr	382			<18	1064			36	212			528			177			896			<18
Ni	145			<2	496			53	98			219			94			372			58
V	322			296	273			372	313			327			307			309			379
Zn	121			127	92			129	118			112			117			96			131
Ce	93			92	56			88	86			82			88			56			112
La	32			32	32			35	213			42			39			25			198
Nb	74			66	35			95	86			73			71			41			96
Ga	21			19	13			22	22			18			21			17			24
Pb	4			<4	4			<4	10			<4			<4			<4			<4
Pr	7			13	<4			16	52			7			10			<4			57
Rb	28			24	17			28	44			26			30			18			27
Ba	323			326	143			414	417			349			314			203			404
Sr	798			829	419			960	938			748			754			501			930
Th	<4			<4	<4			<4	<4			9			<4			<4			5
Y	28			35	17			32	28			30			29			20			30
Zr	311			336	130			389	331			291			297			155			393

[a] Whole-rock (wr) samples are determined by XRF, and fused groundmass (fg) samples are determined by EMP. Major and trace elements are given in weight percent and ppm values, respectively. Fused groundmass compositions represent the average, with standard deviation (σ), of 10 microprobe analyses on different points of the glass shards. Total includes major elements, with all Fe as FeO. Loss on ignition (LOI) values are also listed.

Geochemistry Geophysics Geosystems G3
LONGPRÉ ET AL.: TENO VOLCANISM AND EFFECTS OF LANDSLIDES 10.1029/2009GC002892

Table 2. (continued)

	Sample																				
	TN12,	TN13			TN15			TN16			TN19,	TN27,	TN28,	TN29,	TN30,	TN31,	TN32,	TN33,	TN34,	TN35,	TN36,
	wr	wr	fg	σ	wr	fg	σ	wr	fg	σ	wr	wr	wr	wr	wr	wr	wr	wr	wr	wr	wr
SiO_2	44.23	44.68	45.00	0.56	43.23	44.72	0.57	43.44	45.08	0.78	47.49	47.65	47.54	46.79	47.06	42.94	43.31	43.51	43.07	43.47	64.6
TiO_2	3.94	2.80	3.40	0.20	2.76	4.04	0.18	3.18	3.63	0.26	2.98	3.31	3.32	3.21	3.34	2.49	2.56	3.31	2.59	3.11	0.88
Al_2O_3	15.86	11.93	14.59	0.32	10.09	15.09	0.15	12.51	15.05	0.31	15.66	16.99	16.28	15.35	15.93	9.39	9.68	13.45	9.67	12.74	14.83
FeO_t	12.45	12.41	12.29	0.35	13.40	12.00	0.57	12.06	11.64	0.32	11.99	11.86	11.87	12.17	12.18	12.98	12.88	12.91	12.81	12.65	5.09
MnO	0.17	0.18	0.21	0.03	0.17	0.20	0.05	0.17	0.19	0.05	0.16	0.13	0.13	0.15	0.14	0.20	0.20	0.18	0.19	0.18	0.15
MgO	5.64	12.16	7.54	0.08	16.18	7.20	0.07	11.84	9.87	0.11	5.66	3.66	4.38	4.59	4.53	16.52	16.23	8.95	15.87	10.80	1.28
CaO	10.93	11.84	12.43	0.14	10.04	11.22	0.15	10.31	10.29	0.11	10.83	8.93	9.53	10.01	9.57	10.05	10.28	10.22	10.38	10.58	3.06
Na_2O	3.78	2.21	2.77	0.15	1.73	2.85	0.14	1.96	2.27	0.06	3.02	3.12	2.84	2.68	2.75	1.49	1.58	2.49	1.42	2.12	4.08
K_2O	1.40	0.87	0.94	0.07	0.86	1.18	0.09	0.99	0.96	0.04	0.71	0.97	1.00	0.93	0.89	0.73	0.72	1.24	0.67	1.02	3.39
P_2O_5	0.72	0.39	0.18	0.10	0.42	0.16	0.07	0.48	0.14	0.08	0.39	0.44	0.44	0.44	0.45	0.34	0.36	0.58	0.35	0.50	0.23
Total	99.12	99.47	99.33		98.88	98.67		96.94	99.11		98.89	97.06	97.33	96.32	96.84	97.13	97.80	96.84	97.02	97.17	97.59
LOI	0.82	0.63			0.78			2.73			0.75	1.80	1.74	2.65	2.15	1.29	1.22	1.67	1.66	1.90	2.99
Co	43	67			79			60			49	36	40	46	40	75	71	56	74	55	184
Cr	81	779			1043			657			45	143	98	95	94	1113	1063	355	1087	536	<12
Ni	44	278			495			233			73	72	79	84	88	471	456	194	456	255	–
V	332	305			275			300			278	326	304	286	295	276	279	296	284	309	41
Zn	126	101			106			101			104	94	110	105	107	92	96	106	92	101	106
Ce	90	82			51			86			49	62	60	48	52	40	38	69	46	58	160
La	31	54			43			34			27	15	<14	25	<14	<14	<14	<14	<14	<14	48
Nb	90	52			53			53			40	50	43	46	45	35	35	60	33	49	99
Ga	19	16			14			18			21	23	19	20	22	13	16	20	16	21	20
Pb	7	<4			<4			<4			5	<4	<4	<4	<4	6	6	<4	<4	9	<1
Pr	24	4			<4			13			6	<4	<4	<4	4	<4	<4	7	<4	8	9
Rb	32	18			21			19			15	19	18	13	13	16	14	28	16	21	87
Ba	402	221			251			231			188	246	217	238	258	191	225	322	202	228	621
Sr	958	596			596			622			768	665	641	613	639	418	428	633	415	581	519
Th	<4	<4			<4			<4			<4	<4	<4	<4	<4	<4	<4	<4	<4	<4	16
Y	29	27			20			27			23	30	28	32	30	20	21	29	20	26	42
Zr	375	199			187			234			189	284	220	236	219	177	173	274	170	231	541

Table 3. Rare Earth Element Concentrations Obtained by ICP-MS[a]

Sample	TN3	TN7	TN8	TN10	TN16	TN28	TN32
La	44.70	56.30	49.70	30.80	34.90	28.30	25.30
Ce	93.90	112.90	100.70	61.50	74.00	62.40	54.10
Pr	11.95	13.53	12.34	7.41	8.97	8.04	6.92
Nd	46.90	50.80	46.20	28.20	34.30	32.30	27.30
Sm	9.67	9.57	9.04	5.50	6.90	7.20	5.94
Eu	3.13	2.99	2.82	1.78	2.26	2.34	1.90
Gd	9.02	8.22	7.91	5.16	6.27	6.60	5.44
Tb	1.33	1.17	1.12	0.78	0.94	1.04	0.81
Dy	6.81	5.63	5.54	3.92	4.58	5.18	4.11
Ho	1.24	0.95	0.97	0.71	0.82	1.02	0.73
Er	2.98	2.19	2.29	1.73	2.04	2.35	1.84
Tm	0.42	0.29	0.32	0.24	0.29	0.32	0.26
Yb	2.39	1.61	1.71	1.40	1.63	1.80	1.41
Lu	0.33	0.22	0.24	0.20	0.23	0.26	0.20

[a] Concentrations are in ppm.

of *Thirlwall et al.* [2000] and *Neumann et al.* [1999], were recalculated on a volatile-free basis with all iron as FeO_t prior to plotting. Table 4 lists all samples and their respective stratigraphic position used in this paper.

5.1. Total Alkali-Silica Classification

[27] Most Teno rocks have relatively low SiO_2 and can be classified as alkali basalts, picrites, basanites and subalkali basalts (Figure 6 and Table 4) [cf. *Le Maitre et al.*, 1989; *Le Bas*, 2000; *Thirlwall et al.*, 2000]. However, higher SiO_2 contents are found in a trachyte (sample TN36, the vitric tuff, will be hereinafter referred to as Masca trachytic tuff) and a mugearite (TE53) of the Masca Formation. In addition, the upper Carrizales plagioclase subalkali basalts and a few El Palmar hawaiites, but most notably the much younger Los Gigantes samples TE42, TE44 and TE46 (benmoreites), show comparatively elevated SiO_2. Samples from the two upper formations, the El Palmar and Los Gigantes lavas, display the highest concentrations of alkali elements.

5.2. Major and Trace Element Variations Versus MgO

[28] Major and trace element concentrations and ratios plotted against MgO are presented in Figure 7. While maximum MgO contents measured for Masca and Los Gigantes samples reach ~12 wt %, the postcollapse Carrizales and El Palmar ankaramites contain up to ~17 wt % MgO. As many samples are rich in magnesian olivine and clinopyroxene (see Table 4), it is likely that fractionation and accumulation of these minerals largely control the broad trends above 6 wt % MgO [*Thirlwall et al.*, 2000]. Pronounced inflections at ~6 wt % MgO, especially for SiO_2, TiO_2, FeO_t and CaO, indicate further removal of olivine and clinopyroxene as well as the onset of significant magnetite fractionation. Inflections in Sr concentration and the low P_2O_5 concentrations of the Masca trachytic tuff and Los Gigantes benmoreites point to fractionation of plagioclase and apatite. However, the low-MgO plagioclase basalts (TN27-30) are characterized by rather low Na_2O/Al_2O_3, meaning that plagioclase removal is probably not extensive until MgO < 3–4 wt %. The incompatible trace element ratio zirconium/niobium appears uncorrelated with MgO content. However, for low-MgO samples (e.g., TN36, TE42 and TE46), fractional crystallization of titanite and other accessory phases might have occurred and increased the Zr/Nb ratio [cf. *Ablay et al.*, 1998; *Thirlwall et al.*, 2000]. Groundmass separate compositions fall on the liquid line of descent for all major element oxides except P_2O_5. As this probably is an artifact due to removal of clinopyroxene-hosted apatite microcrystals during groundmass separation [*Longpré et al.*, 2008] or P loss during groundmass melting (A. Klügel, personal communication, 2009), groundmass data points were excluded from the P_2O_5 plot.

5.3. Incompatible Trace Elements

[29] As shown in Figure 7, Zr/Nb is largely insensitive to fractionation of the main silicate minerals. Figure 8a shows that Teno rocks, while having overlapping Zr/Nb and K/Ba (or K/Nb) with Roque

Table 4. Classification of Samples Used in the Geochemical Analysis of This Paper[a]

		UTM (m)			Rock Types		Mineral Modes (%)					
Sample	Location	E	N	Altitude (m)	Field Name	Chemical Name	Ol	Cpx	Plag	Fe-Ti Oxide	Amph	Ne (%)
Los Gigantes												
TE45	A	–	–	1100	basalt	basanite	7	13	0.5	0.5	0.1	9.5
TE44	A	–	–	1085	aphyric basalt	benmoreite		0.2	3	0.3	0.1	5.5
TE42	A	–	–	1080	aphyric basalt	benmoreite			1	0.3	0.4	2.4
TE43	A	–	–	1070	ankaramite	alkali basalt	20	20		0.2	0.1	3.5
TE46	A	–	–	1050	plag. basalt	benmoreite		0.3	40	1	0.2	0.0
TE41	A	–	–	960	basalt	hawaiite		6		2	7	7.4
TE15	A	–	–	680	ankaramite	alkali basalt	15	25		0.5		6.5
TE37	LG	–	–	100	aphyric basalt	alkali basalt	4	0.1				1.2
TE38	LG	–	–	100	basalt	alkali basalt	5	5				2.6
TE39	LG	–	–	100	basalt	alkali basalt	4	6				2.5
TE40	LG	–	–	100	basalt	alkali basalt	5	2				1.7
TN16	–	319620	3126370	4	ankaramite	alkali basalt	15	21	3	1		2.0
El Palmar												
TE24	E	–	–	1100	aphyric basalt	alkali basalt	0.5	1				6.6
TN19	–	321180	3131970	1095	plag. basalt	subalkali basalt	7	3	20			0.0
TE25	E	–	–	1080	ankaramite	picrite	40	30				0.0
TE64	UM	–	–	1080	aphyric basalt	basanite						6.1
TE63	UM	–	–	920	basalt	basanite		4		1.5	4	9.6
TN1	–	317460	3135620	910	ankaramite	alkali basalt	10	18		2		7.0
TF93	–	–	–	–	–	alkali basalt	–	–	–	–	–	6.7
TF94	–	–	–	–	–	alkali basalt	–	–	–	–	–	7.1
TN7	–	318070	3134840	825	ankaramite	alkali basalt	10	13		2		9.4
TE12	UM	–	–	820	aphyric basalt	basanite	0.5	2		1		11.8
TN6	–	318360	3134580	810	aphyric basalt	basanite	0.5	0.5		<0.5		9.4
TE13	UM	–	–	810	ankaramite	picrite	30	30		3		7.7
TN13	–	318390	3133930	800	ankaramite	alkali basalt	20	20				5.0
TN12	–	318020	3134750	795	aphyric basalt	basanite	2	2.9		0.1		10.3
TN11	–	317960	3134580	770	aphyric basalt	alkali basalt	0.2	0.2		0.1		4.8
TE11	UM	–	–	770	basalt	basanite	3	3		0.5		10.2
TN5	–	318970	3134250	765	ankaramite	picrite	30	25				2.9
TE10	UM	–	–	760	aphyric basalt	hawaiite	0.2	0.2				6.3
TN10	–	317960	3134450	750	ankaramite	picrite	23	30		2		4.2
TE62	UM	–	–	750	aphyric basalt	basanite				0.1		9.2
TE9	MM	–	–	750	ankaramite	picrite	35	35				1.4
TN15	–	319720	3132630	730	ankaramite	picrite	27	27		1		3.5
TE8	MM	–	–	710	ankaramite	alkali basalt	10	50	10	5		5.4
TE7	MM	–	–	700	ankaramite	alkali basalt	5	25	5	3		5.9
TN9	–	318060	3134160	695	ankaramite	alkali basalt	28	25		2		5.2
TN8	–	318090	3134110	690	ankaramite	alkali basalt	6	16	4	4		4.1
TE34	NE	–	–	640	ankaramite	alkali basalt	12	25	0.5	1		5.6
TE33	NE	–	–	635	aphyric basalt	hawaiite			2	0.5		0.0
TE35	NE	–	–	635	aphyric basalt	hawaiite	0	0.1	4	0.5		0.0
TE32	NE	–	–	630	ankaramite	alkali basalt	20	30		4		4.8
TE36	NE	–	–	620	ankaramite	alkali basalt	35	25				4.8
TE31	NE	–	–	610	aphyric basalt	alkali basalt	1	1				1.4
TE27	NE	–	–	520	aphyric basalt	alkali basalt	2	1				0.3
TE26	NE	–	–	490	ankaramite	alkali basalt	20	20	25	5		4.1
TE30	NE	–	–	400	aphyric basalt	alkali basalt						4.1
Carrizales												
TN32	–	318990	3133270	785	ankaramite	picrite	23	18	4	<1		2.3
TN31	–	318990	3133270	785	ankaramite	picrite	24	21	5	<1		2.1
TN30	–	318920	3133450	780	plag. basalt	subalkali basalt	<1	5	15			0.0
TN29	–	318920	3133450	775	plag. basalt	subalkali basalt	<1	4	16			0.0
TN28	–	318920	3133450	770	plag. basalt	subalkali basalt	<1	2	23			0.0
TN27	–	318920	3133450	765	plag. basalt	subalkali basalt	1	2	32			0.0
TE61	UM	–	–	750	basalt	alkali basalt	10	0.5				2.0
TN33	–	318370	3133620	745	ankaramite	alkali basalt	12	18	5			4.0
TN34	–	318370	3133620	745	ankaramite	picrite	20	20	5	<1		1.2
TN35	–	318370	3133620	745	ankaramite	alkali basalt	15	20	5			3.0

Table 4. (continued)

Sample	Location	UTM (m) E	UTM (m) N	Altitude (m)	Rock Types Field Name	Rock Types Chemical Name	Mineral Modes (%) Ol	Cpx	Plag	Fe-Ti Oxide	Amph	Ne (%)
TE6	LM	–	–	650	basalt	alkali basalt	3	3				3.9
TE5	LM	–	–	640	aphyric basalt	alkali basalt	0	0.5	3			2.6
TN3	–	316700	3134580	560	aphyric basalt	subalkali basalt	0.3	<0.5	1.5	0.2		0.0
Masca												
TN36	–	320080	3132280	730	vitric tuff	trachyte		2	5	<0.1		0.0
TE4	LM	–	–	460	plag. basalt	alkali basalt	4	0.5	25			3.4
TE3	LM	–	–	400	plag. basalt	subalkali basalt	3	4	10			0.0
TE2	LM	–	–	380	ankaramite	subalkali basalt	25	25				0.0
TE1	LM	–	–	320	aphyric basalt	alkali basalt						2.9
TE52	NW	–	–	120	aphyric basalt	alkali basalt	0.2	0.4	3	0.5		4.0
TE53	NW	–	–	120	plag. basalt	mugearite	0.5		8	0.5		0.9
TE54	NW	–	–	120	basalt	alkali basalt	8	0.2				8.8
TE51	NW	–	–	100	basalt	alkali basalt	4	10				7.9
TE23	NW	–	–	100	basalt	alkali basalt	7	3		0.5		6.5
TF88	–	–	–	–	–	alkali basalt	–	–	–	–	–	9.4

[a] Sample names in normal, italic, and bold refer to samples from *Thirlwall et al.* [2000], *Neumann et al.* [1999], and this paper, respectively. UTM coordinates (our samples) and geographic areas [*Thirlwall et al.*, 2000] are indicated: LM, Lower Masca; MM, Middle Masca; UM, Upper Masca and Teno Alto; NW, NW Teno; E, Erjos; NE, NE Teno; A, Arguayo; and LG, Los Gigantes. Field names, extrapolated from modal mineralogy in the case of samples from *Thirlwall et al.* [2000], and chemical names are compared (Figure 6). Normative nepheline (Ne) was determined using Fe^{3+}/Fe^{2+} calculated after *Kress and Carmichael* [1988] and assuming f_{O2} = QFM+1 [cf. *Gurenko et al.*, 1996; *Klügel et al.*, 2000]. Most samples can be confidently assigned to a specific stratigraphic formation based on locality relative to the observed angular unconformities. Within a particular formation, however, samples are sorted according to altitude. In some cases, true stratigraphic position is therefore uncertain, especially when samples from the same formation were taken in distant areas. Particularly, samples from NW Teno (TE23, TE51–54, and TF88, Masca Formation, Figure 1) are difficult to correlate with samples from Barranco de Masca. Also, it is unclear whether relatively low-altitude samples in the northeast (TE26–27 and TE30–36, El Palmar Formation, Figure 1) are stratigraphically above or below samples from, e.g., the Alto Carrizal–La Tabaiba sequence. No information on locality of sample TE60 of *Thirlwall et al.* [2000] is available; this sample is thus excluded from our analysis. Precise localities for *Neumann et al.*'s [1999] samples are lacking; however, descriptions allow broad correlation to the Masca (TF88) and the El Palmar (TF93 and TF94) formations.

del Conde products, have higher K/Ba than Anaga lavas, though similar Zr/Nb (except for Carrizales lavas, which show higher Zr/Nb). While this implies distinct K/Ba in the sources of Teno and Anaga, Zr/Nb does not seem to vary strongly in the mantle source(s) that supplied Tenerife. On the other hand, the negative correlation of La/Lu and Zr/Nb supports *Thirlwall et al.*'s [2000] use of Zr/Nb as a proxy for (and positively correlated with) the degree of mantle melting at Teno (Figure 8b). First-order batch melting calculations, considering a garnet peridotite source (59.8% olivine, 21.1% orthopyroxene, 7.6% clinopyroxene and 11.5% garnet), standard mineral/melt partition coefficients compiled by *Rollinson* [1993] and primitive mantle Zr and Nb source abundances [*Wood et al.*, 1979], yield Zr/Nb ratios of ~7.7 for a weight fraction of melt (F) < 0.05% and of up to 11.3 for F = 5%. Zr/Nb ratios at Teno are lower (between ~3.3 and 5.8), however. As Zr/Nb remains nearly constant at F < 0.05%, lower Zr/Nb values in Teno samples cannot be explained by even lower melt fractions than modeled here, but rather reflect (1) poorly defined partition coefficients of Zr and Nb [*Thirlwall et al.*, 2000]; (2) a different mineralogy of the source rock, with a possible component of spinel peridotite and/or pyroxenite; and/or (3) different initial concentrations of Zr and Nb in the source rock (e.g., fertile plume component). The results nevertheless imply that mean melt fractions had to be low at Teno, certainly below <3%, consistent with findings of *Thirlwall et al.* [2000]. These authors' modeling, using a different set of parameter values, shows that the range of Zr/Nb ratios at Teno could be produced by 0.1% to ~2% melting of a MORB source, with melts derived from both the garnet and spinel stability fields.

[30] Figure 9a presents normalized rare earth element concentrations for Teno rocks, with stratigraphic formation averages plotted together with the corresponding data range. Despite some overlap, the mean and highest concentrations of REE for a particular formation generally increase from the oldest (Masca) to the youngest (Los Gigantes) lavas, with the notable exception of the Carrizales Formation, which displays lower concentrations in light REE. Indeed, the average La concentration of

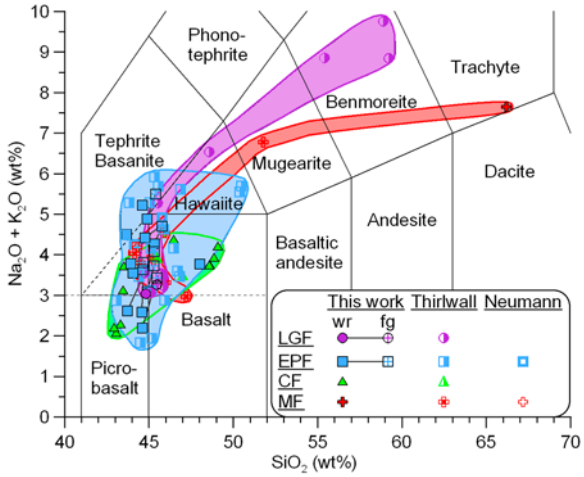

Figure 6. Total alkali-silica chemical classification of Teno rock samples. Data are from *Thirlwall et al.* [2000], *Neumann et al.* [1999], and this work. Color-shaded fields group samples from individual stratigraphic formations (MF, red; CF, green; EPF, blue; and LGF, purple). Here and in Figures 7, 10, and 11, fused groundmass (fg) compositions are linked to their respective whole-rock (wr) chemistry using tie lines. Alkali basalts and subalkali basalts are distinguished based on the presence of nepheline in the CIPW norm (Table 4). Alkali basalt and basanite suites are divided by extrapolation of the tephrite/basanite-hawaiite field boundary (oblique dashed line) [after *Thirlwall et al.*, 2000]. Rocks falling into the picrobasalt and basalt fields that have <3 wt % alkalis (horizontal dashed line) and >12 wt % MgO are picrites (see Table 4) [*Le Bas*, 2000].

El Palmar and Los Gigantes rocks is 1.11 and 1.22 times higher, respectively, than that of Masca samples, whereas the Carrizales Formation La content is only 0.64 times that of Masca. The $(La/Lu)_N$ ratios, which indicate the steepness of the REE patterns, are 17 for Masca, 13 for Carrizales, 20 for El Palmar and 18 for Los Gigantes.

[31] To determine whether these apparent variations are due to fractionation effects or rather reflect the melting process (assuming the Teno mantle source to have had homogeneous REE overall), elements were normalized to the concentration of Lu and Masca ratios were used as reference values (Figure 9b). Thereby largely removing the effects of crystal fractionation [see *Slater et al.*, 1998], this normalization procedure also allows a useful comparison between the different formations of Teno. The data reflect the lower concentration of Carrizales lavas and the higher concentration of El Palmar lavas in the light REE relative to the Masca Formation.

[32] The main observations made in Figures 8 and 9 are therefore the higher Zr/Nb ratios, the lower LREE concentrations and the gentler REE pattern of the Carrizales Formation, suggesting that these lavas were produced by the highest (though still low) degrees of partial melting among the Teno formations.

5.4. Variations With Stratigraphic Level

5.4.1. Entire Teno Sequence

[33] To further investigate the general geochemical evolution of Teno massif, we plotted various proxy parameters as a function of stratigraphic level, using the sequence of samples established in Table 4. A striking feature observed here is the composition of the Masca mugearite and trachytic tuff as well as that of Los Gigantes benmoreites, which show high SiO_2, low Mg # and high Ba, in agreement with extensive crystal fractionation (Figures 10a–10c).

[34] Furthermore, variations in Zr/Nb and normative nepheline with stratigraphy show somewhat similar, though mirrored, patterns (Figures 10d and 10e). Like the Zr/Nb ratio, the degree of silica saturation, expressed as normative nepheline, is thought to be related to the degree of partial melting, as shown by experimental studies [e.g., *Falloon et al.*, 1997, and references therein]. Samples from the Masca Formation in the northwest, inferred to be at the lowest stratigraphic level, show relatively low Zr/Nb and high normative nepheline. Higher up in the Barranco de Masca sequence, Zr/Nb increases and the degree of silica undersaturation decreases, while most Carrizales Formation samples have high Zr/Nb and low or nil normative nepheline. Samples from the northeast, probably at a low stratigraphic level within the El Palmar Formation, also have relatively low normative nepheline, but lower Zr/Nb than upper Carrizales samples. From Alto Carrizal up to an elevation of about 900 m, there is a tendency for increasing normative nepheline and decreasing Zr/Nb. This trend appears to be reversed in the uppermost El Palmar Formation, with some samples at highest altitudes in the region of Cumbre Bolicos showing higher Zr/Nb and lower degrees of silica undersaturation. Los Gigantes lavas at low elevations show similarly high Zr/Nb and low normative nepheline, whereas samples at high altitudes have lower Zr/Nb and display large variations in normative nepheline. Though limited data points are available, La/Lu ratios mimic the variations in normative nepheline (Figure 10f).

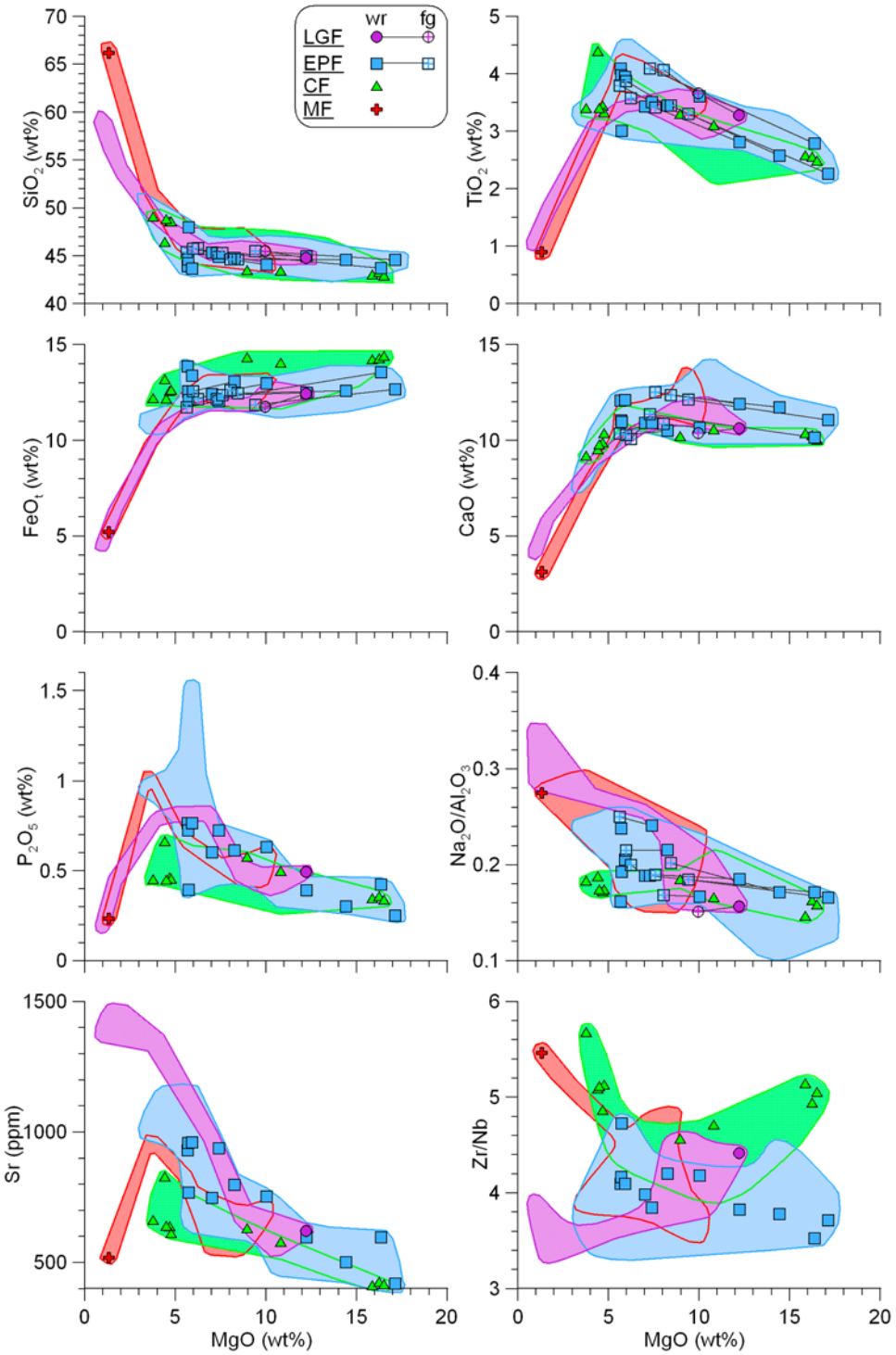

Figure 7. Variation of selected major and trace element concentrations and ratios as a function of MgO content. Fields are as in Figure 6 and include all published Teno data [*Neumann et al.*, 1999; *Thirlwall et al.*, 2000], but only our samples appear as individual symbols for legibility. See section 5.2 for details.

This refines the evidence provided in Figures 8 and 9 and corroborates that peak degrees of partial melting in the mantle, albeit still very modest, were reached during the extrusion of the Carrizales Formation. In addition, this appears to have been followed by a decrease in melt fractions in the mid–El Palmar Formation, in turn followed by a further and seemingly short-lived increase in melt

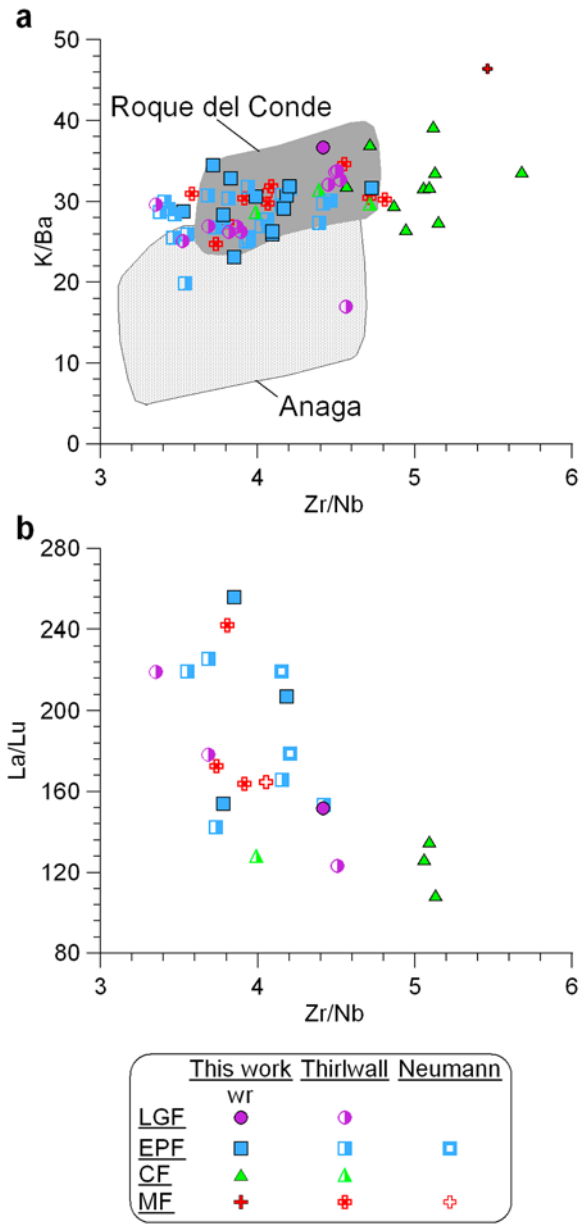

Figure 8. (a) K/Ba versus Zr/Nb for Teno lavas. (b) La/Lu versus Zr/Nb. Data are from *Thirlwall et al.* [2000] (including fields for Roque del Conde and Anaga in Figure 8a), *Neumann et al.* [1999], and this work.

production at the time of extrusion of late El Palmar/early Los Gigantes lavas.

[35] In this context, the bump observed for incompatible elements, such as Ba (Figure 10c) and Sr, in the mid–El Palmar Formation is likely to be in part due to the especially low-fraction melts, yielding higher concentration of these elements. In certain cases, however, crystal fractionation may have played a role, as some of these lavas are relatively differentiated hawaiites.

5.4.2. Detailed Masca–La Tabaiba Sequence

[36] To concentrate our analysis to the potential effects of landslide events on chemical variations, we isolated the well-constrained sampling profile that spans the middle to upper Masca, middle to upper Carrizales and lower to middle El Palmar formations (starting from Barranco de Masca and following the road toward La Tabaiba across both angular unconformities (Figure 11, see also Figure 2)). Note that upper Carrizales ankaramites were excluded from these plots to prevent a sample bias: these ankaramites represent only 5–10% of the rock volume at this stratigraphic level compared to 90–95% for plagioclase basalts (samples TN27–30, see Figures 4c and 5b). In the Barranco de Masca, *Thirlwall et al.*'s [2000] samples TE2, TE3 and

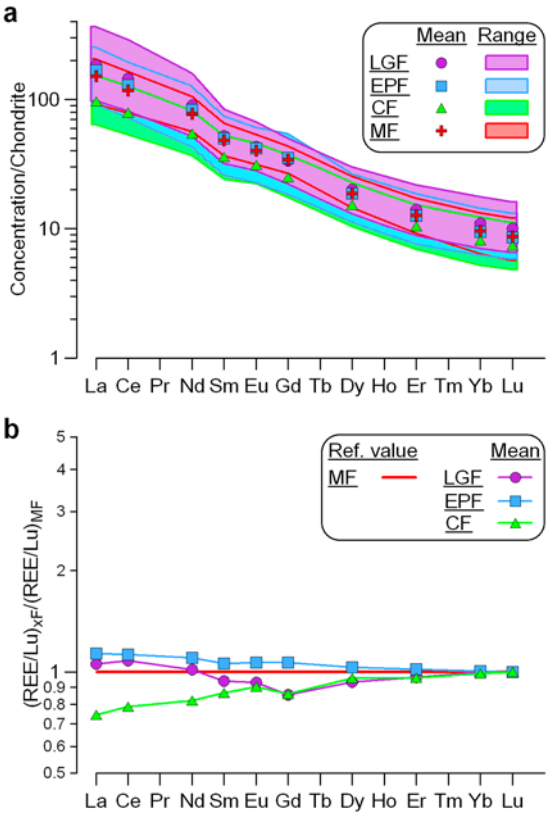

Figure 9. (a) Diagram showing rare earth elements (REE) abundances (normalized to the chondrite values of *Boynton* [1984]) of Teno lavas determined by isotope dilution [*Thirlwall et al.*, 2000] and ICP mass spectrometry [*Neumann et al.*, 1999; this work]. Means and data ranges are presented for each of the stratigraphic formations (MF, 5 samples; CF, 4 samples; EPF, 10 samples; LGF, 4 samples). (b) REE/Lu ratios for Carrizales, El Palmar, and Los Gigantes formations compared to those of the older Masca Formation. See section 5.3 for details.

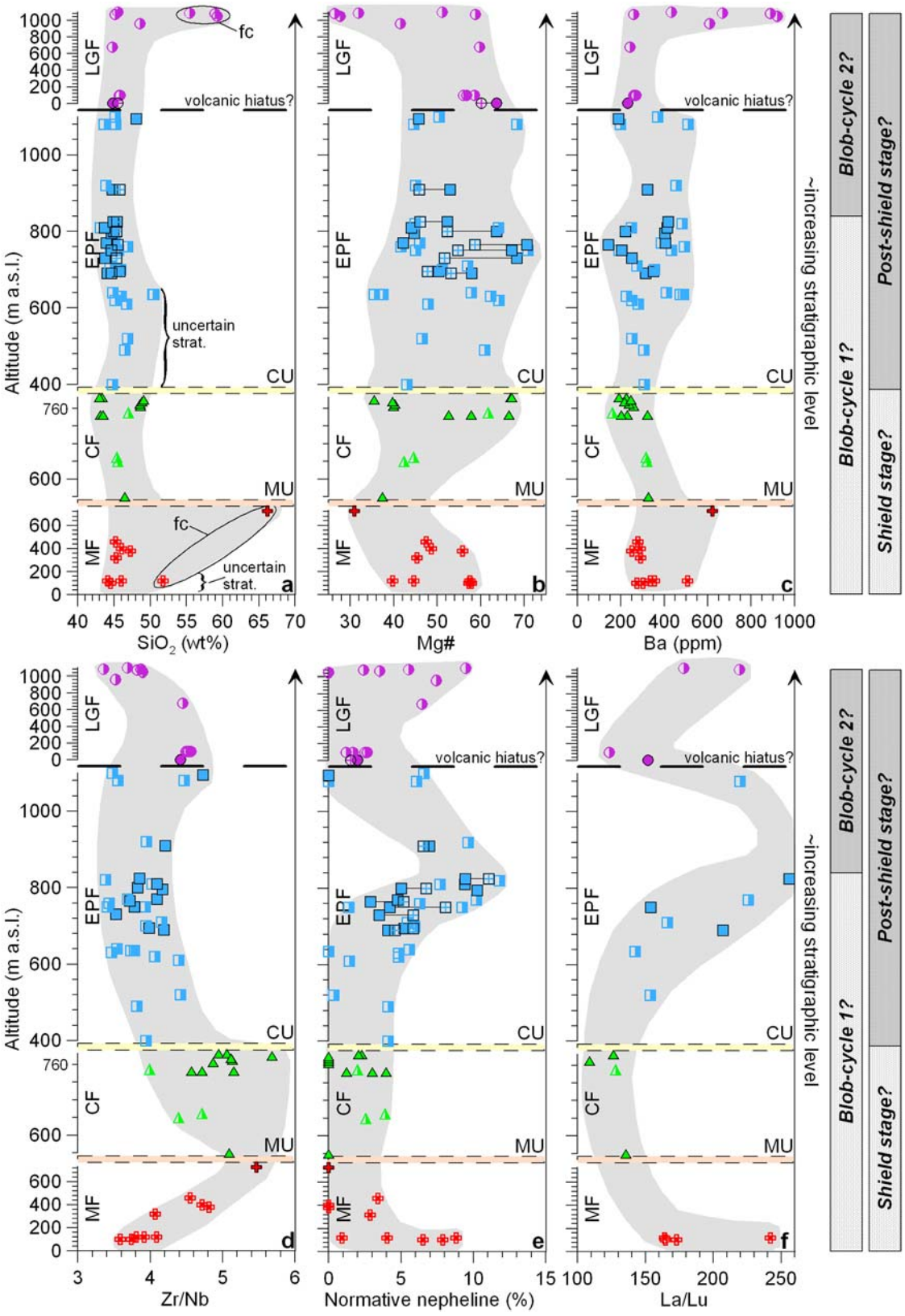
Altitude (m a.s.l.)
LGF
EPF
CF
MF
CU
MU
volcanic hiatus?
uncertain strat.
fc
SiO2 (wt%)
Mg#
Ba (ppm)
Zr/Nb
Normative nepheline (%)
La/Lu
~increasing stratigraphic level
Blob-cycle 2?
Blob-cycle 1?
Post-shield stage?
Shield stage?
a
b
c
d
e
f

Figure 10

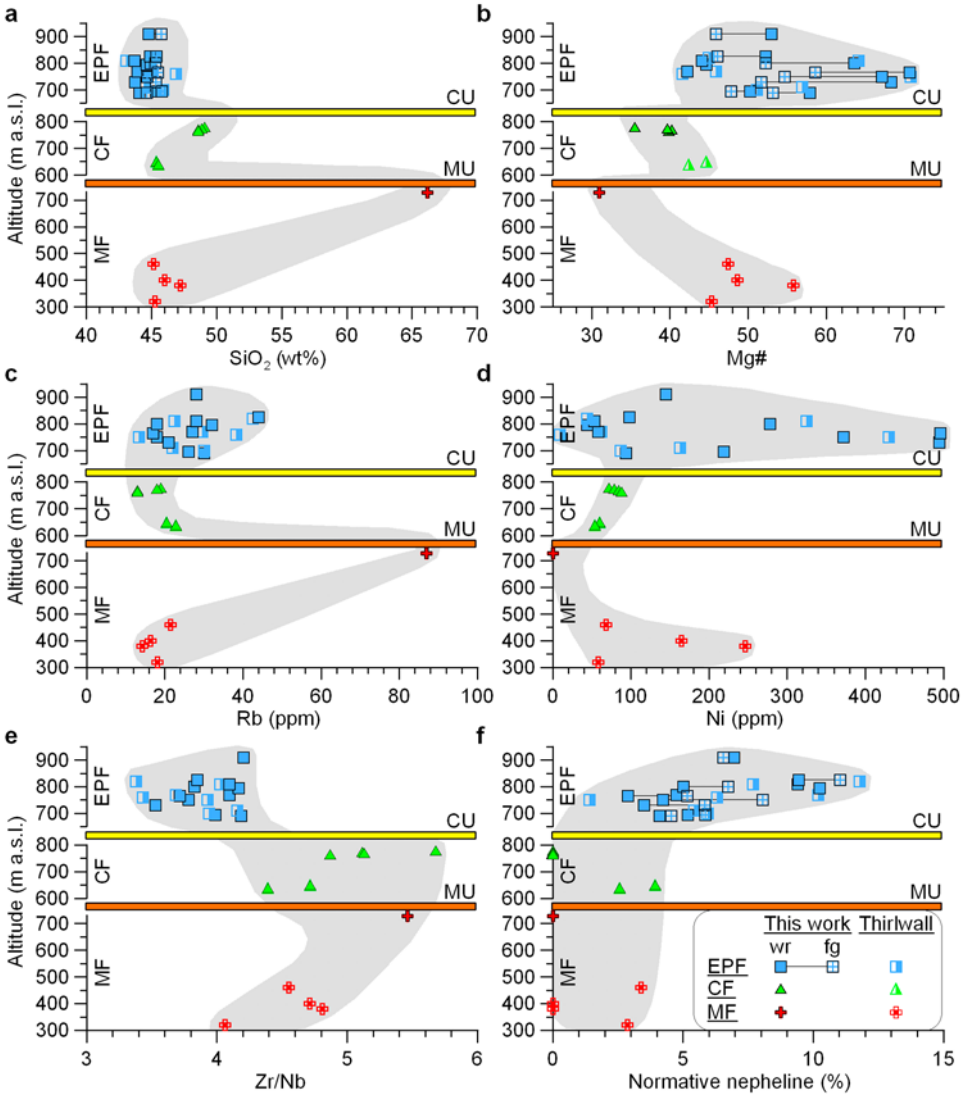

Figure 11. Altitude versus (a) SiO_2, (b) Mg #, (c) Rb, (d) Ni, (e) Zr/Nb, and (f) normative nepheline along the profile from Barranco de Masca to La Tabaiba. All symbols and references [*Neumann et al.*, 1999; *Thirlwall et al.*, 2000; this paper] are as in Figure 6. Stacked *y* axes (as in Figure 10) are used for each of the formations. The position of the angular unconformities, here well constrained, is also indicated, marking the timing of the Teno volcano's giant flank collapses. Shaded bands show proposed geochemical trends (a version of Figure 11 without shaded bands is available in the auxiliary materials). Transitions from relatively high SiO_2 and low–Mg # products to low-SiO_2 and comparatively high Mg # lavas are observed when stepping across each of the unconformities.

Figure 10. Stratigraphic level (indicated by altitude) versus proxy geochemical parameters: (a) SiO_2, (b) Mg #, molar Mg/(Mg + Fe^{total})*100; (c) Ba, (d) Zr/Nb, (e) normative nepheline, and (f) La/Lu. All symbols and references [*Neumann et al.*, 1999; *Thirlwall et al.*, 2000; this work] are as in Figure 6. Each formation has its own *y* axis, the length of which is scaled to the number of samples available for a particular formation. Major (200 m) and minor (40 m) tick marks have constant values in all *y* axes. The approximate position of stratigraphic boundaries (Masca and Carrizales unconformities) is shown, as well as the possible occurrence of a volcanic hiatus between the extrusion of the El Palmar and Los Gigantes formations. Shaded bands show proposed geochemical trends (a version of Figure 10 without shaded bands is available in the auxiliary material). The effect of extensive fractional crystallization (fc) and samples with uncertain stratigraphic position are indicated in Figure 10a. The extent of the shield and postshield stages of evolution or, alternatively, that of possible magmatic cycles is indicated by bars to the right of the diagram. See section 5.4.1 for details.

TE4 show gradually decreasing Mg # and Ni contents and increasing Rb. The Masca trachytic tuff stands out, with anomalously high SiO_2 (64.6 wt %), low Mg # (31, MgO = 1.3 wt %), high Rb and low Ni. Though only reflected by a single analysis to avoid disproportional sampling, this unit implies that the highest degrees of magmatic differentiation, unparalleled at Teno, were reached ''just before'' the Masca Collapse at ~6.1 Ma. Above the Masca Unconformity, mid-Carrizales lavas (average 45.5 wt % SiO_2 and Mg # = 44) are markedly less evolved than the trachytic tuff, but also have lower SiO_2 concentrations and higher Mg # than upper Carrizales plagioclase basalts (average 47.3 wt % SiO_2 and Mg # = 39). This pattern is repeated above the Carrizales Unconformity, whereby lower El Palmar lavas have significantly lower SiO_2 (43.9 wt %) and much higher Mg # (59) and Ni than upper Carrizales samples. Although this must be in part related to accumulated olivine and clinopyroxene phenocrysts in the ankaramites, lower El Palmar groundmass compositions still contain as much as 9.5 wt % MgO (average Mg # = 52). Thus, while moderately to highly differentiated volcanics occur just below each of the collapse unconformitites, a return to more mafic magma compositions is apparent just above these boundaries.

[37] As in Figure 10, the Zr/Nb ratio and normative nepheline are plotted in Figures 11e and 11f. Again, increasing Zr/Nb ratios in the Masca and Carrizales formations are followed by lower values above the Carrizales Unconformity. This is accompanied by increasing normative nepheline in the El Palmar Formation, illustrating declining melt production in the mantle during the extrusion of these lavas. However, as we discuss in section 7.3, these variations are likely unrelated to landslide events.

6. Magma Density Calculations

[38] The ankaramite lavas that were erupted in the lower Carrizales and lower El Palmar formations are intriguing. Such magmas, charged with abundant ferromagnesian phenocrysts, should intuitively be relatively dense. Because magma density may be an important factor controlling the preferential tapping of certain magma types/compositions [e.g., *Stolper and Walker*, 1980; *Pinel and Jaupart*, 2004], we estimated the density of Teno magmas, following the procedure outlined by *Spera* [2000] and using initial volatile contents approximated on the basis of *Dixon et al.* [1997]. That is, dissolved water contents were taken as $H_2O = 3(P_2O_5)$ wt % and initial carbon dioxide as $CO_2 = 2(H_2O)$ by mass. For groundmass samples, we corrected the amount of P_2O_5 according to a linear function of MgO content, based on whole-rock samples that have not experienced apatite removal. Teno samples give a range of $H_2O = 0.75–3$ wt % and $CO_2 = 1.5–6$ wt % [cf. *Dixon et al.*, 1997]. Density calculations were carried out assuming f_{O2} = QFM+1, P = 900 MPa (pressure of main magma storage level [*Longpré et al.*, 2008]), and melts at their liquidus temperature (calculated with PETROLOG [*Danyushevsky*, 2001]). For samples with <10 vol. % olivine + clinopyroxene, the density of the melt was taken as a reasonable approximation of the magma density. For samples with >10 vol. % olivine + clinopyroxene, the magma density was calculated using a melt density of 2870 kg/m^3 (average from fused groundmass samples) and the phenocryst proportions of Table 4 ($\rho_{olivine}$ = 3400 kg/m^3 (~Fo_{80}) and $\rho_{clinopyroxene}$ = 3200 kg/m^3). Plagioclase (due to its density nearly equal to melt density) as well as Fe-Ti oxide and amphibole (due to their small abundances) were considered negligible in these calculations. Results indeed indicate that the crystal-rich ankaramite magmas (ρ = 3060 ± 60 kg/m^3) were substantially denser than magmas that were erupted as aphyric (ρ = 2810 ± 90 kg/m^3), plagioclase-phyric (ρ = 2810 ± 160 kg/m^3) and basaltic (ρ = 2880 ± 60 kg/m^3) lavas. The lowest magma density was obtained from the Masca trachyte TN36 (ρ = 2460 kg/m^3).

7. Discussion

[39] The main results of this study may be summarized as (1) relatively extensive outcrops of pyroclastic rocks are directly associated with the two angular unconformities at several localities in the Teno massif; (2) ankaramite magmas, considerably denser than other Teno magma types, were predominantly erupted in both lower postcollapse sequences, i.e., directly after the landslides in the lower Carrizales and El Palmar formations; (3) early postcollapse lavas are systematically less evolved than late precollapse products; and (4) incompatible trace element and normative nepheline patterns do not show coherent variations with respect to landslide unconformities, but suggest highest (though still very low) degrees of mantle melting during the extrusion of Carrizales lavas.

7.1. Surface Processes and Eruptive Regime

[40] There has not yet been clear consensus on the formation mechanism of the Teno breccias

[*Ancochea et al.*, 1990; *Cantagrel et al.*, 1999; *Walter and Schmincke*, 2002]. Although the blocks (<2 m across) making up the bulk of the breccias are moderately to poorly sorted on the centimeter to meter scale, "megablocks" of tens or even hundreds of meters across, a typical feature of true debris avalanche deposits [e.g., *Siebert*, 1984; *Glicken*, 1996], have not been found at Teno. In addition, the especially thick breccia pile along the road to the east of the Alto Carrizal outcrop consists of several beds in its upper part, hinting toward a more progressive deposition mechanism, at least at this locality. In this context, primary debris avalanche deposits (syn–giant landslide) may not be preserved onshore at Teno (see *Watts and Masson* [1995] for offshore evidence). Instead, the breccias may have largely formed through erosion of the unstable landslide headwall over the course of years to millennia following the successive lateral collapses of the volcano. Similar breccias, also found at the base of a paleolandslide scar on the island of La Gomera, were interpreted likewise [*Paris et al.*, 2005b] and modern analogs may be gradually forming in more recent giant landslide amphitheaters, such as the El Golfo embayment on El Hierro [cf. *Carracedo et al.*, 1999b].

[41] Nevertheless, parts of the breccia successions must have been emplaced rapidly, as suggested by the close association with pyroclastic rocks. At key localities such as the Alto Carrizal and Cherfe outcrops (Figures 2, 4d, 4e, 4f, and 4h), the presence of scoria with fluidal shapes and fiamme-like features strongly suggests that the pyroclasts are juvenile and were deposited hot during explosive eruptions. Although such pyroclastic eruptions may have occurred sometime after the major collapse phase, the position of the lapilli tuffs, dominantly sandwiched between the paleoembayment surface and the breccia pile, advocates for a close temporal association with the actual landsliding event. In this scenario, some of the breccias, consolidated by ashy pyroclastics and adding up to significant thicknesses (e.g., at least 20 m at the Cherfe outcrop), would represent secondary landslides that accompanied pyroclastic eruptions from vents at the base of or on the landslide headwall.

[42] Over the course of Teno's evolution, such explosive activity must have been unusual: apart from some strombolian deposits in the Masca Formation and perhaps areas of the Los Gigantes Formation, pyroclastic rocks are largely restricted to the unconformities and are overall extremely rare in the Teno massif. This suggests a rather drastic effect of both landslides on the upper levels of the volcano's magma plumbing system, with repercussions over a wide region of the failed edifice. Each of the lateral collapses of Teno probably displaced at least 20–25 km^3 of volcanic material, but the area enclosed by the unconformities (33–50 km^2), which is considerably exceeding that of more recent landslide embayments such as Las Playas on El Hierro (8 km^2), may indicate individual volumes in excess of 50 km^3 [cf. *Masson et al.*, 2002; *Walter and Schmincke*, 2002; *Paris et al.*, 2005a]. The giant landslides at the Teno shield may thus have been large enough to rearrange the shallow volcano-tectonic stress field at the nucleus of the rift system [cf. *Walter and Schmincke*, 2002], resulting in widespread explosive activity. Similar claims were made by *Lipman et al.* [1991], who suggested that lateral collapse associated with the formation of the southwest Hawaii slide complex on Mauna Loa may have resulted in sudden, large phreatomagmatic eruptions from the landslide headwall, in an event to some extent analogous to the 18 May 1980 eruption of Mount Saint Helens.

7.2. Magma Plumbing Dynamics

[43] Mass-wasting events of the scale described above, coupled with extensive pyroclastic eruptions, may have ensued initially in shallow magma reservoirs drainage [cf. *Amelung and Day*, 2002; *Longpré et al.*, 2008]. Indeed, while the eruption of felsic pyroclastic material at the mature precollapse volcano, as well as the abundant plagioclase phenocrysts in the upper Carrizales lavas [cf. *Hoernle and Schmincke*, 1993b; *Thirlwall et al.*, 2000], are consistent with crustal level magma storage and differentiation shortly before the flank collapses, evidence for shallow magma storage is scarce throughout the rest of Teno's evolution. *Longpré et al.* [2008] have shown that at least during the emplacement of the El Palmar lavas (and probably for most of the lower Carrizales and Los Gigantes formations as well), the main magma storage zone was located at considerable depth (20–45 km) beneath the volcano, in the uppermost mantle. Crystal fractionation taking place in Teno's magma reservoirs and/or conduits might have been altered by this reconfiguration of the plumbing system after each landslide, in agreement with renewed eruptions of magmas poorer in SiO_2 and characterized by higher Mg # (Figure 11). Analogous flank collapse influences on magma differentiation processes have also been inferred at Waianae

volcano, Hawaii, and at Parinacota, a stratovolcano in northern Chile [*Presley et al.*, 1997; *Ginibre and Wörner*, 2007].

[44] Logging of well-exposed profiles at Teno reveals that the first lavas found at the lowest stratigraphic levels above both collapse unconformities are dominantly ankaramites that are very rich in clinopyroxene and olivine megacrysts up to 3 cm across (Figures 4g, 5a, and 5c). We interpret these lavas to represent remnants of magma batches that have experienced prolonged crystal growth and crystal accumulation at depth, and from which a crystal-poor magma has separated. This is consistent with the groundmass composition of ankaramites, which overlaps with the composition of crystal-poor lavas at Teno (Figures 6 and 7). We thus infer that the formation of ankaramite magmas was an uninterrupted process throughout most of Teno's evolution and that ankaramite dikes and sills were continuously present in the deep plumbing system. However, although ankaramites can be found in all formations and all areas of the massif, it is striking that their relative abundance markedly increases in the lower Carrizales and lower El Palmar formations. We propose that this apparent increased "eruptibility" of ankaramites after flank collapses is related to the change in volcano load. Indeed, *Pinel and Jaupart* [2000, 2004, 2005] have shown that the load of a volcanic edifice induces nonlithostatic stresses that may affect magma reservoir behavior down to depths of about three times the edifice radius. The load of a volcano then acts as a density filter, whereby a growing edifice will progressively impede the eruption of high-density magmas. Eventually, only melts of low density are eruptible. In contrast, edifice destruction will widen the density window of eruptible magmas. This should promote the renewed eruptions of denser, likely more primitive magmas, that had stalled beneath the edifice, also in agreement with recent analog models [*Kervyn et al.*, 2009]. Therefore, while Teno's growth and increasing load favored magma stagnation and eruption of differentiated magmas in late precollapse times, rapid unloading of several tens of km^3 of near-surface rocks, for both the Masca and Carrizales collapses, will have facilitated the tapping of high-density ankaramite magmas.

[45] Moreover, because Canarian mafic magmas are volatile saturated at high pressure (>1000 MPa) and exsolve a CO_2-dominated vapor phase, an unloading-induced depressurization of the magma storage environment on the order of a few megapascals may thus have been sufficient to enhance bubble formation and CO_2 degassing at depth [*Pinel and Jaupart*, 2005]. According to our estimated bulk volatile contents, Teno's ankaramite magmas may have had as much as 0.8 to 2.1 wt % H_2O and 1.5 to 4.3 wt % CO_2 prior to ascent, eruption and associated degassing [cf. *Dixon*, 1997; *Dixon et al.*, 1997; *Hansteen et al.*, 1998]. At Teno, this may have resulted in a gas exsolution–magma density feedback, further promoting the remobilization and rapid ascent of dense and mafic ankaramite magmas previously trapped at depth [cf. *Longpré et al.*, 2008]. In addition, recent numerical models by *Manconi et al.* [2009] show that volcano flank collapses can induce pressure gradients within deep magma plumbing systems, providing another mechanism for stirring and remobilization of stagnant ankaramite magma batches. We emphasize that considerable disturbance of the magma plumbing system is likely to ensue directly from growth and destruction of the volcano, essentially following the numerical and physical arguments of *Pinel and Jaupart* [2000, 2005].

7.3. Mantle Source, Partial Melting, and Magmatic Cycles

[46] The mantle source(s) of Roque del Conde, Teno and Anaga must have had distinct K/Nb, K/Ba and isotopic ratios [*Simonsen et al.*, 2000; *Thirlwall et al.*, 2000]. However, largely overlapping Zr/Nb in these basaltic shields implies little variation in this elemental ratio in the overall mantle source. The variations in Zr/Nb at Teno, on the other hand, can be explained by different amounts of low-degree (<3%) partial melting in the mantle. Using the Zr/Nb proxy for partial melting, *Thirlwall et al.* [2000] noted that the geochemistry of Teno lavas was consistent with a progressively waning melt fraction through time [see *Thirlwall et al.*, 2000, Figure 12]. However, additional sampling and the recognition of unconformity-bounded stratigraphic units reveal a slightly more complicated picture. As shown earlier, patterns in Zr/Nb (Figures 8 and 10d), normative nepheline (Figure 10e) and REE (Figures 9 and 10f) rather suggest slightly higher degrees of partial melting during the emplacement of the Carrizales Formation, more than 0.2 Ma after Teno's first subaerial emissions. This was followed by a gradual decrease in melt fractions during the extrusion of lower to middle El Palmar lavas, in turn followed by apparent fluctuations in the melting regime. Two possible scenarios that may account for these observations

are discussed below: (1) partial melting variations at Teno were controlled by long-term, intrinsic plume processes and mark a transition from the shield stage (Masca and Carrizales lavas) to the postshield stage (El Palmar and Los Gigantes lavas) of volcanic growth [e.g., *Frey et al.*, 1990], with possible involvement of successive mantle blobs [cf. *Hoernle and Schmincke*, 1993a], or (2) magma generation was affected by extrinsic factors operating on short time scales; that is, repeated partial edifice destruction through lateral collapses, during a single magmatic cycle, gave rise to partial melting fluctuations [e.g., *Presley et al.*, 1997; *Hildenbrand et al.*, 2004].

7.3.1. Intrinsic Plume Processes

[47] The increasing alkalinity of Teno lavas and the eruption of hawaiites and basanites in the El Palmar and Los Gigantes formations mimic the changes defined to mark the shield stage/postshield stage transition at some Hawaiian volcanoes (Figures 6 and 10 and Table 4). Declining melt fractions in the mantle at this point would thus reflect the migration of the volcano away from the hot spot locus [e.g., *Frey et al.*, 1990]. In this scenario, the older Masca and Carrizales formations would represent the peak of the shield activity, when the volcano was close to the plume center and magma supply was highest due to maximum melt production.

[48] Alternatively, apparent fluctuations in the degree of melting inferred from variations of Zr/Nb, normative nepheline and REE may be attributed to two successive blob-induced melting cycles (Figures 10d–10f) [cf. *Hoernle and Schmincke*, 1993a]. Beginning near the time of emergence of Teno above sea level, the melting of a main blob may have produced the Masca, Carrizales and the better part of El Palmar magmas. In this context, the Carrizales Formation would originate from melts formed in the hotter center of this blob, where highest degrees of partial melting result in the least silica-undersaturated magmas. One may hypothesize that a second, much smaller blob cycle may be responsible for the uppermost El Palmar lavas and the Los Gigantes Formation. However, further testing is required to determine whether the "blob model" is viable for Tenerife as a whole.

7.3.2. Extrinsic Factors: Flank Collapses

[49] Because mantle melting under Canarian volcanoes is thought to be due to decompression of upwelling plume material [*Hoernle and Schmincke*, 1993a, 1993b], variations in pressure due to the addition or subtraction of a surface load (volcanic construction/destruction) may result in feedback-related changes in the rate and degree of mantle melting, if the effect of such loading/unloading "propagates" down to the melting region. A useful analogy may be that of ice sheet loading/unloading during glaciation/deglaciation periods in Iceland that had drastic effects on volcanism there [*Hardarson and Fitton*, 1991; *Sigvaldason et al.*, 1992; *Jull and McKenzie*, 1996; *Slater et al.*, 1998; *Maclennan et al.*, 2002]. Indeed, after reduced melt generation during glaciation, ice unloading at the end of the last ice age resulted in a prodigious increase of melt generation in the shallow Icelandic mantle and accelerated eruption rates by a factor of 30. Postglacial lavas were found to show greater range of and generally higher MgO with significantly lower light REE concentrations [*Slater et al.*, 1998; *Maclennan et al.*, 2002].

[50] The Icelandic case differs considerably from other hot spot settings such as Hawaii, Society or the Canary Islands. Due to the interactions between a mantle plume and a spreading ridge, the young Icelandic crust and lithosphere are warmer and more ductile than the older and colder oceanic lithosphere under typical ocean island volcanoes. At intraplate hot spots, however, there is a significant mechanical boundary layer and the melting zone is thus thinner and restrained at much greater depth, i.e., mostly in the spinel and garnet stability fields between about ~70–140 km depth, compared to ~20–115 km at Iceland [e.g., *Watson and McKenzie*, 1991; *Hoernle and Schmincke*, 1993b; *Jull and McKenzie*, 1996]. In addition, while deglaciation actually removes ice over a large area, flank collapse redistributes the failed rock mass and affects a smaller area.

[51] At Teno, the short time interval of ~250 ka between the last deposits of the Masca Formation, the successive giant landslides and subsequent extrusion of scar-infilling Carrizales and El Palmar lavas [*Leonhardt and Soffel*, 2006] is compatible with high magma supply and increased rate of melt generation in the mantle following the volcano flank collapses. However, while the geochemical features of Carrizales lavas could be the result of enhanced decompressional melting due to the Masca Collapse, El Palmar lavas do not bear a similar signature of increased partial melting that, in this context, would be expected after the Carrizales Collapse.

[52] *Presley et al.* [1997] argued that a decompression of about 100–200 MPa in the interior of Waianae volcano, on Oahu, Hawaii, after a large

mass-wasting event (the Waianae slump) might have been sufficient to cause a ~1% increase in melt generation in the melting region at depth. This would explain the differences between the preslump (Palehua Member) and postslump (Kolekole) lavas. Similar claims were made by *Hildenbrand et al.* [2004] for Tahiti-Nui Island (French Polynesia). The latter authors attributed an increase in eruptive rate, as well as variation in certain trace elements, to have been caused by increased mantle melting, as a result of a decompression response to lateral collapse of the volcanic edifice. However, *Presley et al.* [1997], in their melting calculations, simply transpose near surface decompression (at the base of the slump) to the melting region (at >70 km depth). The analysis of *Manconi et al.* [2009] indicates that the decompression induced by volcano flank collapses decrease rapidly with depth [see also *Pinel and Jaupart*, 2000] and that at a depth of only 20 km below the seafloor, decompression associated with a Waianae-sized landslide (some ~6000 km^3) is already below 20 MPa. Thus, decompression due to large-scale landslides seems unlikely to reach the melting zone beneath oceanic hot spot volcanoes in magnitudes sufficient to cause a detectable increase in melt production.

7.4. An Evolutionary Model for the Teno Volcano

[53] Although the possibility that Teno's melt production regime may have been influenced by collapse-induced decompression cannot be fully ruled out at this stage, we favor a model in which long-term variations in the degrees of partial melting were controlled by intrinsic plume processes. While Teno was characterized by a somewhat typical hot spot volcano evolution (keeping in mind the extreme tectonic setting of the Canary Islands [e.g., *Hoernle and Schmincke*, 1993a, 1993b; *Carracedo et al.*, 1998]), its eruptive regime and magma plumbing dynamics were perturbed by volcano load and large-scale mass-wasting events. Indeed, the landslide-induced changes at Teno appear to have extended all the way from the surface (increase in pyroclastic activity) through the deep magma plumbing system (sudden disappearance of evolved products, increase in eruptions of more mafic and denser magmas stored at uppermost mantle levels). Independent pieces of evidence from different volcanic systems and from theoretical and experimental arguments have started to form a more coherent picture [e.g., *Presley et al.*, 1997; *Pinel and Jaupart*, 2005; *Kervyn et al.*, 2009; *Manconi et al.*, 2009; this paper] and it seems likely that constructive and destructive processes may play a role so far underestimated in regulating the short-term geochemical regimes of several ocean island volcanoes.

[54] On the basis of the data presented, we propose a model for the evolution of the Teno volcano (Figure 12):

[55] From about 6.3 to 6.1 Ma ago, alternation of phreatomagmatic and effusive basaltic eruptions constructed the initially steep, subaerial Teno edifice (Figure 12a). At this stage, melt generation rates in the upper mantle, though modest, were comparatively high for this volcano. Sustained magma supply, coupled with the effect of volcano load, may have permitted the formation of shallow magma reservoirs, presumably within the volcanic edifice, where some of Teno's most evolved (trachytic) magmas were produced. These highly differentiated, low-density magmas were erupted once Teno had reached a significant size and its northern slopes became unstable.

[56] Eventually, after a phase of gradual flank creep, the northern flank of Teno failed ~6.1 Ma ago (Figure 12b), producing a U-shaped embayment some 5–10 km across. This resulted in the depressurization of the shallow magma reservoir(s), leading to widespread explosive eruptions from vents at the base of, or on the landslide headwall. These pyroclastic eruptions occurred contemporaneously with secondary landslides, probably associated with rapid erosion of the landslide headwall closely following the main landslide event. Shallow magma reservoirs have largely been drained at that point.

[57] The decompression effect of this first giant landslide also affected the volcano's deep plumbing system. Remobilization and tapping of dense, crystal-rich magmas, which had previously accumulated at uppermost mantle levels, was facilitated by volcano unload (Figure 12c). This resulted in the rapid filling of the Masca Collapse embayment by the less evolved, near-horizontal Carrizales lavas that were initially mostly ankaramites. The volcano being at the peak of its subaerial shield stage, melt generation, presumably within the spinel and garnet stability fields, reached a maximum at this point (low degrees of silica undersaturation, high Zr/Nb and low La/Lu). Rapid volcano regrowth and associated lava pile load (at least 200–300 m thick, but plausibly reached as much as 700 m in thickness [cf. *Walter and Schmincke*, 2002]) eventually started to impede the ascent of

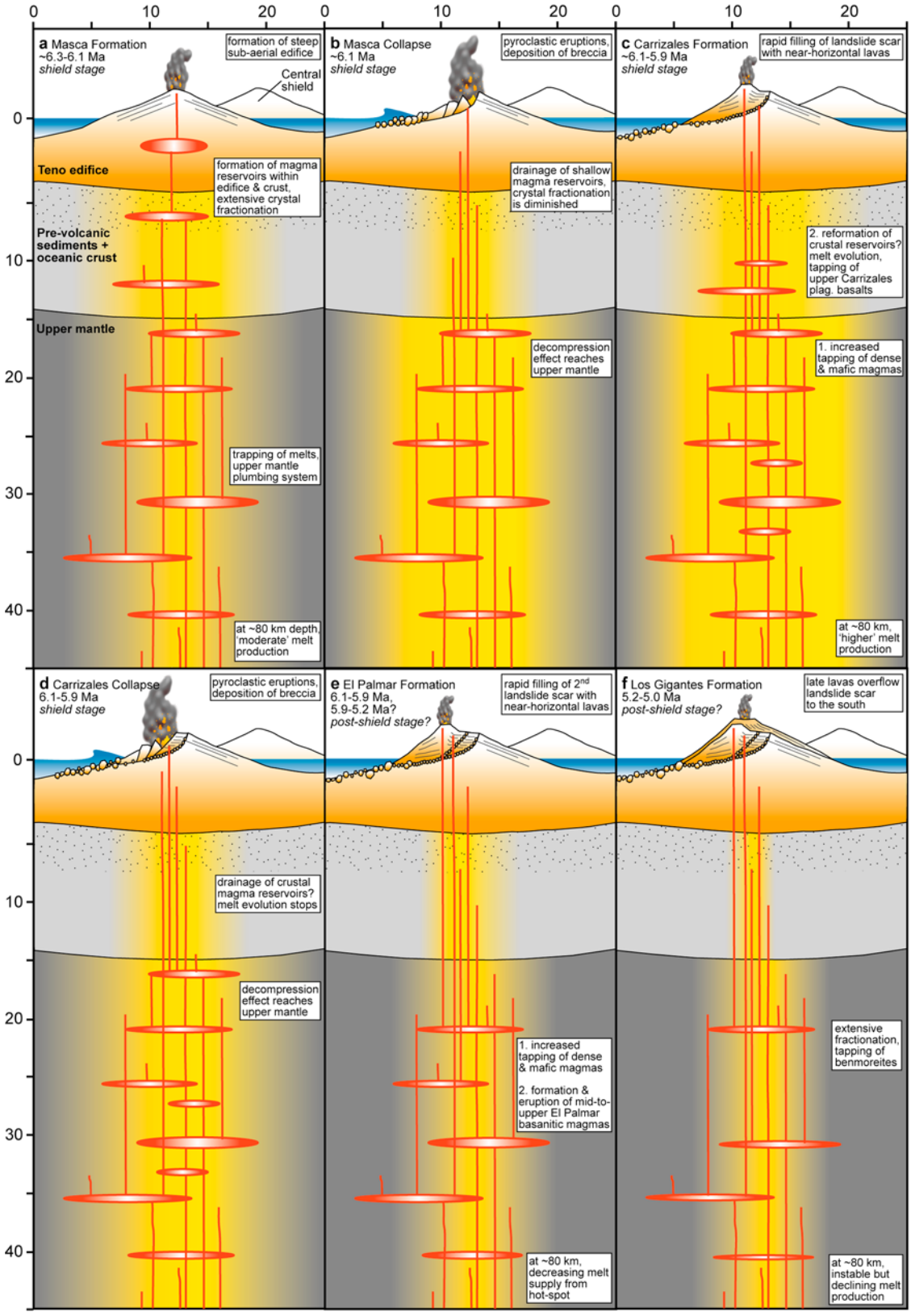

Figure 12. Conceptual model of the evolution of the Teno volcano. Depth and horizontal distance values are in kilometers. The height of the volcanic edifice is exaggerated. Magma storage depth range is caricatured from results of *Longpré et al.* [2008] and this work. See section 7.4 for details.

dense ankaramite magmas. Magma stagnation and evolution, perhaps in crustal magma chambers, produced significant volumes of lower-density plagioclase-phyric basalts that were able to erupt.

[58] Flank instability resumed in the north. After renewed periods of flank creep, the Carrizales lava pile collapsed seaward, forming a second giant landslide embayment (Figure 12d). As in the case of the first collapse, widespread pyroclastic eruptions were closely associated with landsliding; lapilli tuffs and polymict breccias were deposited on the walls of the landslide amphitheater.

[59] The deep plumbing system was once more disturbed by surface unloading; plagioclase basalts, abundant in the upper pre–Carrizales Collapse sequence, virtually disappeared after this landslide. Again, dense ankaramite magmas were preferentially tapped in the early postcollapse eruptive episode (Figure 12e). The mean melt fractions started to decrease shortly after this second collapse, and this may have been due to the overall declining influence of the hot spot as the volcano entered the more alkalic postshield stage of development. Eruptions of ankaramites were eventually followed by the emissions of crystal-poor basanite lavas. During this phase, magma storage took place in the upper mantle [*Longpré et al.*, 2008], and there is no evidence for prolonged storage of magmas at shallow depths. Both giant landslides and subsequent embayment infill took place in a geologically very short time, probably within ~250 ka, from ~6.1 to 5.9 Ma ago.

[60] The uppermost part of the El Palmar Formation (largely eroded today) may have been emplaced nearly contemporaneously to Teno's youngest Miocene lavas (5.2–5.0 Ma), the Los Gigantes Formation, that overflowed the filled collapse embayment (Figure 12f), although a hiatus in activity is suggested by magnetostratigraphy [*Leonhardt and Soffel*, 2006]. Instability in the melting region may have resulted in temporally restricted fluctuations in melt fractions late in the postshield stage of this volcano. Some Los Gigantes lavas were the product of substantial degrees of magma differentiation, not encountered since the precollapse, upper Masca Formation. Magma supply eventually became too low and Miocene magma conduits shut off.

8. Conclusions

[61] The main conclusions of this study are as follows:

[62] 1. Extensive explosive volcanism was closely associated with both large-scale lateral collapses of the Teno volcano in the late Miocene.

[63] 2. Some of Teno's most evolved magmas were produced just prior to giant landslide events. Less differentiated, denser magmas frequently charged with large olivine and clinopyroxene phenocrysts, were erupted "immediately" after the large-scale collapses.

[64] 3. The lavas of the Carrizales Formation were probably derived from higher mean mantle melt fractions than the other stratigraphic formations of Teno: however, this does not seem related to the landslide events.

[65] 4. We propose that while the increasing load of the mature precollapse volcano has encouraged magma stagnation and differentiation, the giant lateral collapses have rearranged the shallow volcano-tectonic stress field, resulting in widespread pyroclastic activity that drained shallow magma reservoirs. The redistribution of tens of km^3 of near-surface rocks seems to have been sufficient in transmitting a substantial pressure decrease at depth, which in turn facilitated the remobilization and ascent of dense, crystal-rich magmas stored at upper mantle levels. We prefer a model where the overall variation in melt production at Teno is explained by intrinsic plume processes, rather than by collapse-induced decompression. A transition from the volcano's peak shield-building stage (Carrizales Formation) to its postshield stage may have taken place early during the extrusion of the El Palmar Formation.

[66] 5. This case study of the Teno volcano adds to a growing body of evidence, suggesting that constructive and destructive processes may play a role yet underappreciated in regulating the eruptive regime, the magma plumbing dynamics and, thereby, the short-term geochemical evolution of many ocean island volcanoes.

Acknowledgments

[67] We thank G. Nicoll (TCD) for assistance in the field, G. Brey (U. Frankfurt) for organizing the shock-melting experiment logistics, and M. Thöner (IFM-GEOMAR) for EMP analytical support. We are grateful to E. Holohan (UCD), A. Manconi (GFZ Potsdam), and G. Wörner (U. Göttingen) for discussions and suggestions that helped to improve the manuscript. This paper also benefited from thoughtful reviews by J. Maclennan, A. Klügel, J. Dixon, J. C. Carracedo, and an anonymous reviewer. M. Thirlwall, R. Paris, H. Guillou, and R. Leonhardt kindly provided details of their sampling locali-

ties. V.R.T. acknowledges early discussions with A. Klügel, H.-U. Schmincke, J. C. Carracedo, and H. Clarke. Financial support was provided through a Natural Science and Engineering Research Council of Canada Scholarship and a Trinity Postgraduate Studentship to M.-A.L. and by Trinity College Dublin and Science Foundation Ireland to V.R.T.

References

Abdel-Monem, A., N. D. Watkins, and P. W. Gast (1972), Potassium-argon ages, volcanic stratigraphy, and geomagnetic polarity history of the Canary Islands; Tenerife, La Palma and Hierro, *Am. J. Sci.*, *272*(9), 805–825.

Ablay, G. J., M. R. Carroll, M. R. Palmer, J. Martí, and R. S. J. Sparks (1998), Basanite-phonolite lineages of the Teide-Pico Viejo volcanic complex, Tenerife, Canary Islands, *J. Petrol.*, *39*(5), 905–936, doi:10.1093/petrology/39.5.905.

Amelung, F., and S. J. Day (2002), InSAR observations of the 1995 Fogo, Cape Verde, eruption: Implications for the effects of collapse events upon island volcanoes, *Geophys. Res. Lett.*, *29*(12), 1606, doi:10.1029/2001GL013760.

Ancochea, E., J. M. Fuster, E. Ibarrola, A. Cendrero, J. Coello, F. Hernan, J. M. Cantagrel, and C. Jamond (1990), Volcanic evolution of the island of Tenerife (Canary Islands) in the light of new K-Ar data, *J. Volcanol. Geotherm. Res.*, *44*(3–4), 231–249, doi:10.1016/0377-0273(90)90019-C.

Anguita, F., and F. Hernán (2000), The Canary Islands origin: A unifying model, *J. Volcanol. Geotherm. Res.*, *103*(1–4), 1–26, doi:10.1016/S0377-0273(00)00195-5.

Boynton, W. V. (1984), Geochemistry of the rare earth elements: Meteorite studies, in *Rare Earth Element Geochemistry*, edited by P. Henderson, pp. 63–114, Elsevier, Amsterdam.

Cande, S. C., and D. V. Kent (1995), Revised calibration of the geomagnetic polarity timescale for the Late Cretaceous and Cenozoic, *J. Geophys. Res.*, *100*(B4), 6093–6095, doi:10.1029/94JB03098.

Cantagrel, J. M., N. O. Arnaud, E. Ancochea, J. M. Fuster, and M. J. Huertas (1999), Repeated debris avalanches on Tenerife and genesis of Las Cañadas caldera wall (Canary Islands), *Geology*, *27*(8), 739–742, doi:10.1130/0091-7613(1999)027<0739:RDAOTA>2.3.CO;2.

Carracedo, J. C., S. J. Day, H. Guillou, E. Rodríguez Badiola, J. A. Canas, and F. J. Pérez Torrado (1998), Hotspot volcanism close to a passive continental margin: The Canary Islands, *Geol. Mag.*, *135*(5), 591–604, doi:10.1017/S0016756898001447.

Carracedo, J. C., S. J. Day, H. Guillou, and P. Gravestock (1999a), Later stages of volcanic evolution of La Palma, Canary Islands: Rift evolution, giant landslides, and the genesis of the Caldera de Taburiente, *Geol. Soc. Am. Bull.*, *111*(5), 755–768, doi:10.1130/0016-7606(1999)111<0755:LSOVEO>2.3.CO;2.

Carracedo, J. C., S. J. Day, H. Guillou, and F. J. Pérez Torrado (1999b), Giant Quaternary landslides in the evolution of La Palma and El Hierro, Canary Islands, *J. Volcanol. Geotherm. Res.*, *94*(1–4), 169–190, doi:10.1016/S0377-0273(99)00102-X.

Carracedo, J. C., E. Rodríguez Badiola, H. Guillou, J. de la Nuez, and F. J. Pérez Torrado (2001), Geology and volcanology of La Palma and El Hierro, western Canaries, *Estud. Geol.*, *57*, 175–273.

Carracedo, J. C., E. Rodríguez Badiola, H. Guillou, M. Paterne, S. Scaillet, F. J. Pérez Torrado, R. Paris, U. Fra-Paleo, and A. Hansen (2007), Eruptive and structural history of Teide Volcano and rift zones of Tenerife, Canary Islands, *Geol. Soc. Am. Bull.*, *119*(9–10), 1027–1051, doi:10.1130/B26087.1.

Clague, D. A., and G. B. Dalrymple (1987), The Hawaiian-Emperor volcanic chain. Part I. Geologic evolution, in *Volcanism in Hawaii*, edited by R. W. Decker, T. L. Wright, and P. H. Stauffer, *U.S. Geol. Surv. Prof. Pap.*, *1350*, 5–54.

Danyushevsky, L. V. (2001), The effect of small amounts of H_2O on crystallisation of mid-ocean ridge and backarc basin magmas, *J. Volcanol. Geotherm. Res.*, *110*(3–4), 265–280, doi:10.1016/S0377-0273(01)00213-X.

Day, S. J., S. I. N. Heleno da Silva, and J. F. B. D. Fonseca (1999), A past giant lateral collapse and present-day flank instability of Fogo, Cape Verde Islands, *J. Volcanol. Geotherm. Res.*, *94*(1–4), 191–218, doi:10.1016/S0377-0273(99)00103-1.

Dixon, J. E. (1997), Degassing of alkalic basalts, *Am. Mineral.*, *82*(3–4), 368–378.

Dixon, J. E., D. A. Clague, P. Wallace, and R. Poreda (1997), Volatiles in alkalic basalts from the North Arch volcanic field, Hawaii: Extensive degassing of deep submarine-erupted alkalic series lavas, *J. Petrol.*, *38*(7), 911–939, doi:10.1093/petrology/38.7.911.

Falloon, T. J., D. H. Green, H. S. C. O'Neill, and W. O. Hibberson (1997), Experimental tests of low degree peridotite partial melt compositions: Implications for the nature of anhydrous near-solidus peridotite melts at 1 GPa, *Earth Planet. Sci. Lett.*, *152*(1–4), 149–162, doi:10.1016/S0012-821X(97)00155-6.

Frey, F. A., W. S. Wise, M. O. Garcia, H. West, S. T. Kwon, and A. Kennedy (1990), Evolution of Mauna Kea volcano, Hawaii: Petrologic and geochemical constraints on post-shield volcanism, *J. Geophys. Res.*, *95*(B2), 1271–1300, doi:10.1029/JB095iB02p01271.

Gee, M. J. R., A. B. Watts, D. G. Masson, and N. C. Mitchell (2001), Landslides and the evolution of El Hierro in the Canary Islands, *Mar. Geol.*, *177*(3–4), 271–293, doi:10.1016/S0025-3227(01)00153-0.

Ginibre, C., and G. Wörner (2007), Variable parent magmas and recharge regimes of the Parinacota magma system (N. Chile) revealed by Fe, Mg and Sr zoning in plagioclase, *Lithos*, *98*(1–4), 118–140, doi:10.1016/j.lithos.2007.03.004.

Glicken, H. (1996), Rockslide-debris avalanche of May 18, 1980, Mount St. Helens volcano, Washington, *U.S. Geol. Surv. Open File Rep., 96-677*, 90 pp.

Guillou, H., J. C. Carracedo, R. Paris, and F. J. Pérez Torrado (2004), Implications for the early shield-stage evolution of Tenerife from K/Ar ages and magnetic stratigraphy, *Earth Planet. Sci. Lett.*, *222*(2), 599–614, doi:10.1016/j.epsl.2004.03.012.

Gurenko, A. A., T. H. Hansteen, and H.-U. Schmincke (1996), Evolution of parental magmas of Miocene shield basalts of Gran Canaria (Canary Islands): Constraints from crystal, melt and fluid inclusions in minerals, *Contrib. Mineral. Petrol.*, *124*(3–4), 422–435, doi:10.1007/s004100050201.

Hansteen, T. H., A. Klügel, and H.-U. Schmincke (1998), Multi-stage magma ascent beneath the Canary Islands: Evidence from fluid inclusions, *Contrib. Mineral. Petrol.*, *132*(1), 48–64, doi:10.1007/s004100050404.

Hardarson, B. S., and J. G. Fitton (1991), Increased mantle melting beneath Snaefellsjoekull volcano during Late Pleistocene deglaciation, *Nature*, *353*(6339), 62–64, doi:10.1038/353062a0.

Hildenbrand, A., P. Y. Gillot, and I. Le Roy (2004), Volcano-tectonic and geochemical evolution of an oceanic intra-plate

volcano: Tahiti-Nui (French Polynesia), *Earth Planet. Sci. Lett.*, *217*(3–4), 349–365, doi:10.1016/S0012-821X(03)00599-5.

Hoernle, K., and H.-U. Schmincke (1993a), The role of partial melting in the 15-Ma geochemical evolution of Gran Canaria: A blob model for the Canary Hotspot, *J. Petrol.*, *34*(3), 599–626.

Hoernle, K., and H.-U. Schmincke (1993b), The petrology of the tholeiites through melilite nephelinites on Gran Canaria, Canary Islands: Crystal fractionation, accumulation, and depths of melting, *J. Petrol.*, *34*(3), 573–597.

Holik, J. S., P. D. Rabinowitz, and J. A. Austin (1991), Effects of Canary hotspot volcanism on structure of oceanic crust off Morocco, *J. Geophys. Res.*, *96*(B7), 12,039–12,067, doi:10.1029/91JB00709.

Jull, M., and D. McKenzie (1996), The effect of deglaciation on mantle melting beneath Iceland, *J. Geophys. Res.*, *101*(B10), 21,815–21,828, doi:10.1029/96JB01308.

Kervyn, M., G. G. J. Ernst, B. van Wyk de Vries, L. Mathieu, and P. Jacobs (2009), Volcano load control on dyke propagation and vent distribution: Insights from analogue modeling, *J. Geophys. Res.*, *114*, B03401, doi:10.1029/2008JB005653.

Klügel, A., K. A. Hoernle, H.-U. Schmincke, and J. D. L. White (2000), The chemically zoned 1949 eruption on La Palma (Canary Islands): Petrologic evolution and magma supply dynamics of a rift zone eruption, *J. Geophys. Res.*, *105*(B3), 5997–6016, doi:10.1029/1999JB900334.

Kress, V. C., and I. S. E. Carmichael (1988), Stoichiometry of the iron oxidation reaction in silicate melts, *Am. Mineral.*, *73*(11–12), 1267–1274.

Le Bas, M. J. (2000), IUGS reclassification of the high-Mg and picritic volcanic rocks, *J. Petrol.*, *41*(10), 1467–1470.

Le Maitre, R. W., P. Bateman, A. Dudek, J. Keller, L. Lameyre, P. Sabine, R. Schmidt, H. Sorensen, W. A. R. Streckeisen, and B. Zanettin (1989), *A Classification of Igneous Rocks and Glossary of Terms: Recommendations of the International Union of Geological Sciences Subcommission on the Systematics of Igneous Rocks*, 193 pp., Blackwell Sci., Oxford, U. K.

Leonhardt, R., and H. C. Soffel (2006), The growth, collapse and quiescence of Teno volcano, Tenerife: New constraints from paleomagnetic data, *Int. J. Earth Sci.*, *95*(6), 1053–1064, doi:10.1007/s00531-006-0089-3.

Lipman, P. W., J. M. Rhodes, and G. B. Dalrymple (1991), The Ninole Basalt—Implications for the structural evolution of Mauna Loa volcano, Hawaii, *Bull. Volcanol.*, *53*(1), 1–19, doi:10.1007/BF00680316.

Longpré, M.-A., V. R. Troll, and T. H. Hansteen (2008), Upper mantle magma storage and transport under a Canarian shield-volcano, Teno, Tenerife (Spain), *J. Geophys. Res.*, *113*, B08203, doi:10.1029/2007JB005422.

Maclennan, J., M. Jull, D. McKenzie, L. Slater, and K. Grönvold (2002), The link between volcanism and deglaciation in Iceland, *Geochem. Geophys. Geosyst.*, *3*(11), 1062, doi:10.1029/2001GC000282.

Manconi, A., M.-A. Longpré, T. R. Walter, V. R. Troll, and T. H. Hansteen (2009), The effects of flank collapses on volcano plumbing systems, *Geology*, *37*(12), 1099–1102, doi:10.1130/G30104A.1.

Masson, D. G., A. B. Watts, M. J. R. Gee, R. Urgeles, N. C. Mitchell, T. P. Le Bas, and M. Canals (2002), Slope failures on the flanks of the western Canary Islands, *Earth Sci. Rev.*, *57*(1–2), 1–35, doi:10.1016/S0012-8252(01)00069-1.

McGuire, W. J. (1996), Volcano instability: A review of contemporary themes, in *Volcano Instability on the Earth and Other Planets*, edited by W. J. McGuire, A. P. Jones, and J. Neuberg, *Geol. Soc. Spec. Publ.*, *110*, 1–23.

Moore, J. G., W. R. Normark, and R. T. Holcomb (1994), Giant Hawaiian landslides, *Annu. Rev. Earth Planet. Sci.*, *22*(1), 119–144, doi:10.1146/annurev.ea.22.050194.001003.

Neumann, E.-R., E. Wulff-Pedersen, S. L. Simonsen, N. J. Pearson, J. Martí, and J. Mitjavila (1999), Evidence for fractional crystallization of periodically refilled magma chambers in Tenerife, Canary Islands, *J. Petrol.*, *40*(7), 1089–1123, doi:10.1093/petrology/40.7.1089.

Oehler, J. F., J. F. Lénat, and P. Labazuy (2008), Growth and collapse of the Reunion Island volcanoes, *Bull. Volcanol.*, *70*(6), 717–742, doi:10.1007/s00445-007-0163-0.

Paris, R., J. C. Carracedo, and F. J. Pérez Torrado (2005a), Massive flank failures and tsunamis in the Canary Islands: Past, present, future, *Z. Geomorph.*, *140*, suppl., 37–54.

Paris, R., H. Guillou, J. C. Carracedo, and F. J. Pérez Torrado (2005b), Volcanic and morphological evolution of La Gomera (Canary Islands), based on new K-Ar ages and magnetic stratigraphy: Implications for oceanic island evolution, *J. Geol. Soc.*, *162*(3), 501–512, doi:10.1144/0016-764904-055.

Pinel, V., and C. Jaupart (2000), The effect of edifice load on magma ascent beneath a volcano, *Philos. Trans. R. Soc. A*, *358*(1770), 1515–1532.

Pinel, V., and C. Jaupart (2004), Likelihood of basaltic eruptions as a function of volatile content and volcanic edifice size, *J. Volcanol. Geotherm. Res.*, *137*(1–3), 201–217, doi:10.1016/j.jvolgeores.2004.05.010.

Pinel, V., and C. Jaupart (2005), Some consequences of volcanic edifice destruction for eruption conditions, *J. Volcanol. Geotherm. Res.*, *145*(1–2), 68–80, doi:10.1016/j.jvolgeores.2005.01.012.

Presley, T. K., J. M. Sinton, and M. Pringle (1997), Postshield volcanism and catastrophic mass wasting of the Waianae Volcano, Oahu, Hawaii, *Bull. Volcanol.*, *58*(8), 597–616, doi:10.1007/s004450050165.

Rollinson, H. R. (1993), *Using Geochemical Data: Evaluation, Presentation, Interpretation*, 352 pp., Longman Sci. and Tech., Essex, U. K.

Siebert, L. (1984), Large volcanic debris avalanches: Characteristics of source areas, deposits, and associated eruptions, *J. Volcanol. Geotherm. Res.*, *22*(3–4), 163–197, doi:10.1016/0377-0273(84)90002-7.

Sigvaldason, G. E., K. Annertz, and M. Nilsson (1992), Effect of glacier loading/deloading on volcanism: Postglacial volcanic production rate of the Dyngjufjöll area, central Iceland, *Bull. Volcanol.*, *54*(5), 385–392, doi:10.1007/BF00312320.

Simonsen, S. L., E. R. Neumann, and K. Seim (2000), Sr-Nd-Pb isotope and trace-element geochemistry evidence for a young HIMU source and assimilation at Tenerife (Canary Island), *J. Volcanol. Geotherm. Res.*, *103*(1–4), 299–312, doi:10.1016/S0377-0273(00)00228-6.

Slater, L., M. Jull, D. McKenzie, and K. Gronvöld (1998), Deglaciation effects on mantle melting under Iceland: Results from the northern volcanic zone, *Earth Planet. Sci. Lett.*, *164*(1–2), 151–164, doi:10.1016/S0012-821X(98)00200-3.

Smith, J. R., and P. Wessel (2000), Isostatic consequences of giant landslides on the Hawaiian Ridge, *Pure Appl. Geophys.*, *157*, 1097–1114, doi:10.1007/s000240050019.

Spera, F. J. (2000), Physical properties of magma, in *Encyclopedia of Volcanoes*, edited by H. Sigurdsson et al., pp. 171–190, Academic, San Diego, Calif.

Stolper, E., and D. Walker (1980), Melt density and the average composition of basalt, *Contrib. Mineral. Petrol.*, *74*(1), 7–12, doi:10.1007/BF00375484.

Thirlwall, M. F., B. S. Singer, and G. F. Marriner (2000), ^{39}Ar-^{40}Ar ages and geochemistry of the basaltic shield stage of Tenerife, Canary Islands, Spain, *J. Volcanol. Geotherm. Res.*, *103*(1–4), 247–297, doi:10.1016/S0377-0273(00)00227-4.

Tibaldi, A. (2004), Major changes in volcano behaviour after a sector collapse: Insights from Stromboli, Italy, *Terra Nova*, *16*(1), 2–8.

Walter, T. R., and H.-U. Schmincke (2002), Rifting, recurrent landsliding and Miocene structural reorganization on NW-Tenerife (Canary Islands), *Int. J. Earth Sci.*, *91*(4), 615–628, doi:10.1007/s00531-001-0245-8.

Walter, T. R., V. Acocella, M. Neri, and F. Amelung (2005a), Feedback processes between magmatic events and flank movement at Mount Etna (Italy) during the 2002–2003 eruption, *J. Geophys. Res.*, *110*, B10205, doi:10.1029/2005JB003688.

Walter, T. R., V. R. Troll, B. Cailleau, A. Belousov, H.-U. Schmincke, F. Amelung, and P. van den Bogaard (2005b), Rift zone reorganization through flank instability in ocean island volcanoes: An example from Tenerife, Canary Islands, *Bull. Volcanol.*, *67*(4), 281–291, doi:10.1007/s00445-004-0352-z.

Watson, S., and D. McKenzie (1991), Melt generation by plumes: A study of Hawaiian volcanism, *J. Petrol.*, *32*(3), 501–537.

Watts, A. B., and D. G. Masson (1995), A giant landslide on the north flank of Tenerife, Canary Islands, *J. Geophys. Res.*, *100*(B12), 24,487–24,498, doi:10.1029/95JB02630.

White, J. D. L., and B. F. Houghton (2006), Primary volcaniclastic rocks, *Geology*, *34*(8), 677–680, doi:10.1130/G22346.1.

Wood, D. A., J. L. Joron, M. Treuil, M. Norry, and J. Tarney (1979), Elemental and Sr isotope variations in basic lavas from Iceland and the surrounding ocean floor, *Contrib. Mineral. Petrol.*, *70*(3), 319–339, doi:10.1007/BF00375360.